Remote Detection of a Lunar Granitic Batholith at Compton-Belkovich

Matthew Siegler (msiegler@psi.edu)
Planetary Science Institute https://orcid.org/0000-0002-7940-3931
Jianqing Fang
Planetary Science Institute
Katelyn Lehman-Franco
Southern Methodist University
Jeffrey Andrews-Hanna
Southwest Research Institute
Rita Economos
Southern Methodist University
Michael St. Clair
Million Concepts
Chase Million
Million Concepts
James Head III
Brown University
Timothy Glotch
Stony Brook University https://orcid.org/0000-0002-8187-3609
Mackenzie White
Southern Methodist University

Physical Sciences - Article

Keywords:

Posted Date: October 26th, 2022

DOI: https://doi.org/10.21203/rs.3.rs-2043330/v1

Title: Remote Detection of a Lunar Granitic Batholith at Compton-Belkovich

Authors: Matthew A. Siegler[1*], Jianqing Feng[1*], Katelyn Lehman-Franco[2], Jeffery C. Andrews-Hanna[3], Rita C. Economos[2], Michael St. Clair[4], Chase Million[4], James W. Head[5], Timothy D. Glotch[6], Mackenzie N. White[2]

Affiliations:

[1] Planetary Science Institute, Tucson, AZ, 85719

[2] Southern Methodist University, Dallas, TX, 75275

[3] University of Arizona, Tucson, AZ, 85721

[4] Million Concepts, Louisville, KY, 40204

[5] Brown University, Providence, RI, 02912

[6] SUNY Stony Brook, Stony Brook, NY 11794

Corresponding Authors: Matthew A Siegler (msiegler@psi.edu), Jianqing Feng (jfeng@psi.edu)

Abstract:

Granites are nearly absent in the Solar System outside of Earth. Achieving granitic compositions in magmatic systems requires multi-stage melting and fractionation, which also increase radiogenic element concentrations. Water and plate tectonics facilitate these processes on Earth, aiding in remelting. Although these drivers are absent on the Moon, small granite samples have been found, but details of their origin and the scale of systems they represent are unknown. We report microwave-wavelength measurements of an anomalously hot geothermal source that is best explained by the presence of a ~50 km diameter granitic system below the thorium-rich, farside feature known as Compton-Belkovich. Passive microwave radiometry is sensitive to the integrated thermal gradient to several wavelengths depth. The 3-37 GHz antenna temperatures of the Chang'E 1 and 2 microwave instruments allow us to measure peak heat flux of ~184 mWm^{-2}; ~20 times higher than the average lunar highlands. The surprising magnitude and geographic extent of this feature imply an Earth-like, evolved granitic system larger than believed possible on the Moon, especially outside of the Procellarum region. Furthermore, these methods are generalizable: similar uses of passive radiometric data could vastly expand our knowledge of geothermal processes on the Moon and other planetary bodies.

Article

Granitic rocks are common on Earth due in part to the presence of water and plate tectonics which aid in melting and recycling crustal materials. Igneous systems elsewhere in the Solar System are dominated by basalt, representing single-stage melting of mantle rock. Granite production requires multi-stage remelting of basalt or crystal fractionation of basaltic liquids. These processes also drive an increased concentration of incompatible elements such as Si and radiogenic K, Th, and U[1]. Rare granitic clasts found in lunar samples contain high radiogenic concentration, suggested to represent extrusive volcanism [2]. However, the origin and scale of systems that produced them are unknown. Lunar silicic volcanic materials, found primarily in the nearside Procellarum region [3], are generally coincident with high gamma-ray detected Th concentrations [4,5]. Still, there is little to constrain subsurface structures and processes that created these systems.

An enigmatic, farside feature known as Compton-Belkovich (C-B) [4,6] has the highest localized Th concentrations on the Moon. Located at 61.2° N, 99.7° E between its two namesake craters, Compton-Belkovich has been mapped as a likely volcanic or plausibly impact-related feature [7-11] . Here, we present the discovery that a large granitic batholith, similar in volume to terrestrial batholiths such as the Andean Altiplano-Puna Magma Body [12] underlays Compton-Belkovich. We identify this C-B batholith through a broad, increased local geothermal heat flux, which peaks at ~150-200 mWm^{-2} — approximately 20 times that of the background lunar highlands [13] and over eight times that measured at the anomalously hot Apollo 15 site. Such high heat flux requires a large mid-crustal body with much higher radiogenic element concentrations than previously observed from orbit [4]. Here we detail evidence based on a combination of models and data from the Chang'E-1 (CE-1) and 2 (CE-2) orbiters, NASA's Lunar Reconnaissance Orbiter, and past data from the Lunar Prospector, GRAIL, Chandrayaan-1, and Apollo missions.

[Figure 1 here]

The Chang'E 1 and 2 orbiters carried four-channel (3-37 GHz) microwave radiometer instruments. These data provide near-global coverage over most of the diurnal cycle, including 8 CE-1 and 13 CE-2 passes over C-B. Maps presented here are generally from CE-2, which had a lower orbit and therefore higher spatial resolution. MRM data are an antenna temperature (*TA*), which results from emitted brightness temperatures (*Tb*) as seen by the instrument field of view. **Figure 1** shows 3 GHz midnight antenna temperature in the C-B region (after latitudinal trends have been removed), revealing an enhancement of ~9K, coincident with the Th-anomaly. A similar "hotspot" is observed at all frequencies, at all local times, in both Chang'E 1 and 2 microwave data [Methods]. We find this brightness temperature anomaly can only be explained by an enhanced geothermal gradient, also providing the first example of a new technique that could provide a window into the interior compositions of the Moon and other planetary bodies.

Compton-Belkovich consists of a central, ~15 km diameter plain ringed by three kilometer-scale domes [7]. The high-albedo interior displays a short-wavelength infrared Christiansen feature consistent with a silicic surface [8], which is proposed evidence of erupted rhyolitic lavas [7-9]. Interior to the domes, several groups have mapped what appear to be circumferential faulting suggestive of a piston-style collapsed caldera [9,10]. These features have been hypothesized to mark the edge of a once-inflated magma body, potentially now evacuated, approximately 13 km in diameter. The greater region surrounding C-B shows an enhanced Th concentration, postulated to be an ashfall deposit [6], leading to estimates of erupted materials' volume and plausible water content [14]. However, previous studies have been limited to studying the surface signature of the volcanism, making indirect inferences regarding what lies beneath.

Microwave radiometry provides a means to peer below the surface to measure the integrated subsurface physical temperature. The measurement frequency and the dielectric properties (summarized by the loss tangent, which is the ratio between the real and imaginary dielectric constants) [15,16] controls the depth over which materials add to the emitted radiance. Lower frequencies (longer wavelengths) and lower loss tangents will sense heat from greater depths. Conversely, higher frequencies and higher loss tangents will sense temperatures closer to the surface.

[Figure 2 Here]

On Earth, water's high dielectric loss limits microwave penetration. The Moon, Mars, and other planetary bodies with dry conditions, regolith cover, and low atmospheric pressure exhibit extremely low loss tangents (<0.01), enabling microwave remote sensing to greater depths. Furthermore, the low thermal conductivity of the lunar regolith ($<10^{-3}$ $Wm^{-1}K^{-1}$) both shallows diurnal temperature variations (to the upper ~50 cm) and provides high geothermal gradients (>1 K/m) [17]. Consequently, increases in temperature with depth due to the geothermal gradient will increase measurable brightness temperatures, with a stronger signal at lower frequencies. **Figure 2** illustrates the relationship between (**2a**) the modeled gradient from various geothermal fluxes, (**2b**) the weighting function over which emitted heat is integrated for each Chang'E frequency, and (**2c**) the resulting increase in relative brightness temperature as a function of heat flux (dashed lines represent 10% variation in loss tangent).

We find no plausible explanation for high antenna temperatures other than an enhanced subsurface geothermal heat source. Low albedo can cause higher brightness temperatures, but C-B is higher albedo than its surroundings. Changes in near-surface density or loss tangent will alter the diurnal *Tb* amplitude [16], but higher *Tb* are seen at all local times. We find the C-B feature is similar in near-surface density and loss to the surrounding region, with a loss tangent of ~0.005-0.01 [Methods]. With these losses, 3 GHz measurements should be sensitive to heat within the upper ~5.5 m [16].

The antenna temperature obtained by a microwave radiometer depends on the instrument radiation pattern (the angular dependence of power density). Using a multi-frequency fit at two altitudes (~200 km for CE-1 and ~100 km for CE-2) and instrument antenna patterns [see Methods], we can use the variable resolution to characterize the magnitude, size, and shape of the heat source. First, we create a forward model of subsurface emission from solar heating, fit to LRO Diviner infrared measurements accounting for effects of slope, azimuth, density, LRO Diviner rock abundance, and loss tangents fit from Chang'E data [see Methods]. Then we apply a frequency-dependent antenna pattern to the forward model of the emitted microwave radiance, converting from modeled *Tb* to *TA*. The resulting antenna temperature models provide a good fit for temperature variations due to topography and surface geology, but reveal a strong brightness temperature excess in both CE-1 and CE-2 data at C-B [Methods] seen at all frequencies (Shown in Figure 3).

[Figure 3 Here]

While this enhancement's location coincides with the increased surface Th observed at C-B [6], it is a much larger increase than explainable by surface materials. Previous orbital measurements estimate C-B to have up to ~49 ppm Th [4], higher than all but a few lunar samples [18]. 150 mWm^{-2} would require a layer of roughly 20 km of such material, neglecting any lateral heat conduction. In reality, heat will spread into the surrounding crust, so 49 ppm Th would require an even thicker deposit, exceeding the ~50 km crustal column [19]. This lateral spread of heat flux helps define the size and depth of the heat source, as a wider or deeper source would increase the spread by the conduction of heat through the crust. While there is a trade-off between the source depth, size, and radiogenic element concentration, we can provide bounds by examining remote sensing, samples, and petrologic data.

The evidence of Th-rich silicic volcanism from remote sensing, geomorphology, and Th-rich granites and quartz-monzodiorites within the Apollo samples lead to a reasonable assertion that C-B may be underlain by a granitic body [5,9-11]. Therefore, we attempt to fit the residual antenna temperature increase with a forward model of a discrete subsurface geothermal heat source assuming a geometry of an elliptical pluton. We give crustal material outside C-B commonly assumed heat production values [20], resulting in a surface flux of ~8 mWm^{-2}. To match the observed brightness temperatures and geometry, we begin with a 13 km wide ellipsoidal body at 1 km depth. To provide a peak heat flux of 150-200 mWm^{-2} on the surface would require ~50-68 $\times 10^{-6}$ Wm^{-3} of heat production. However, this is about 2.3-3.1 times the heat production of the most radiogenic materials found in lunar samples [18], equivalent to ~400 ppm Th. Such a highly radiogenic body is neither plausible, nor would such a source explain the broad shape of the heat source needed to fit the data.

To examine reasonable source materials, we look to Apollo samples. High-Th lunar samples fall into three classes: 35-44 ppm Th quartz-monzodiorites (here labeled G_A) [21,22], ~62-70 ppm Th granites (G_B) [18, 21, 23], and a single, highly-evolved Apollo 12 granite sample with 132 ppm Th (G_C) [23]. Using the G_C clast as an upper limit of potential lunar radiogenic composition, we model a highly concentrated ellipsoid ~1km below C-B underlain by a deeper, less-radiogenic (G_B) and much larger body. Furthermore, a second body is a sensible assumption as it would provide a lower-Th, intermediate-stage reservoir from which to distill the upper pluton. In reality, the lower body is likely composed of several intermediate chambers and sills [Methods], with this ellipsoidal shape approximating their net heat production and gravity.

With this simplified geometry (assuming 2:1 ellipsoid aspect ratios), we tested ~600 model variations in upper/lower pluton sizes. For 10-20 km diameter upper plutons, solutions for the lower body fall within a narrow trade space, with diameters of 47 and 57 km [Methods]. Our favored model retains the upper G_C pluton as 13 km in diameter at 1km depth with a second G_B body that is ~53 km in diameter at ~7.5 km depth (centered at 20.5 km depth). The resulting heat flux peaks at 184 mWm^{-2}, making this the highest detected heat flux on the Moon, approximately 20 times the 5-10 mWm^{-2} highlands background[13]. **Figure 2d** illustrates our favored model heat flux for each pluton, their combination (top), and the modeled antenna temperature increase that would occur (bottom). **Figure 3** shows the fit of the curves in 2d to the Chang'E data. Our two bodies represent up to 1.7 % of the total lunar Th-budget estimated from surface concentrations [13].

Figure 4 illustrates the resulting temperature and heat flux from our modeled pluton. In **Figures 4b-d**, we find a peak temperature of 867 K within the lower pluton, placing it below the liquidus at present, but feasibly molten in the past. Heat sources assuming quartz-monzodiorite (G_A composition) required bodies the scale of the entire 50 km crustal column and would result in a much wider surface expression. Deeper, larger G_B concentration bodies also produce a more laterally extensive surface heat flux than is consistent with the data, again requiring a mid-crustal heat source. This heat flux could warm nighttime surface temperatures by ~1K, but we cannot detect this signal among effects of local topography and albedo in LRO Diviner data [Methods].

GRAIL Bouguer gravity data reveals a narrow positive gravity anomaly centered on and comparable in scale to the microwave brightness anomaly on the shoulder of the broader Compton-Belkovich region Bouguer gravity high. Although it is impossible to uniquely constrain the density structure due to the large regional gravity anomalies, we can test whether the favored pluton model is consistent with the observed gravity. The modeled gravity arising from this pluton model matches the observed anomaly for density contrasts of the lower body ranging from 60–120 kg/m^3 relative to the surroundings, with the density anomaly of the upper body assumed to be half that of the lower body. These density contrasts equate to absolute densities of 2940-3000 kg/m^3 and 2470-2500 kg/m^3 for the lower and upper bodies, respectively, based on a linear density model for the farside highlands [24]. Assuming a low porosity, the density of the lower body implies a material that is somewhat less dense than typical mare [25], consistent with a slightly more silicic composition, while the low density of the upper body suggests a more evolved and silicic intrusion. **Figure 4 e-f** show the effect of removing the gravity anomaly from a model assuming a 90 kg/m^3 density anomaly for the lower batholith from the observed gravity.

[Figure 4 Here]

These data solidify the conclusion that Compton-Belkovich is the result of felsic volcanism and provide evidence for an evolved magma plumbing system much larger than expected on the Moon [1,3,5 6, 11, 26]. A magmatic system of this size requires one of the following features: (a) a long-lived thermal source, such as a farside mantle plume (which appears in some models [27]), to facilitate multi-stage magmatic processing, (b) an anomalously wet pocket of the otherwise dry Moon (consistent with C-B volcanic estimates of 2 wt.% water [14]) which could lower the local melting point, or (c) a farside KREEP layer that could build sufficient radiogenic material to remelt through self-heating. All scenarios imply large-scale compositional heterogeneities in the mantle and/or crust during lunar formation.

Petrogenesis of lunar granites, "felsites," and quartz monzodiorites is subject to ongoing debate centered around four models: (1) differentiation driven by silicate-iron liquid immiscibility [28,29], (2) remelting of lunar crust in large impact events [30], (3) crystal fractionation of KREEP basaltic liquids [31, 32, 33], and (4) partial melting of KREEP-rich monzogabbro and alkali gabbronorite crust [34]. Hypothesis 1 is precluded at C-B due to the lack of correlation between high Th contents and a large positive Bouguer gravity anomaly, as Th would fractionate into the denser, iron-rich component [34]. The system's geometry required to accommodate the observed heat flow anomalies precludes Hypothesis 2. Thus, both remaining scenarios, or likely a combination of the two, require the initial presence of a farside KREEP component to form the C-B system. The distillation of radiogenic elements via remelting or crystal fractionation from KREEP components is needed to achieve the U and Th compositions that produce the observed heat flow feature. The KREEP-rich material beneath Compton-Belkovich may represent a local thickening of a former continuous farside KREEP layer or a relict patch of KREEP left behind after a global layer was remobilized to the nearside[35].

Furthermore, this work represents the first mapping of the lunar geothermal gradient from orbit through passive microwave radiometry, which can provide a new window into crustal and interior heat-producing structures. The high heat flux and relatively low-loss material at Compton-Belkovich allowed the multiple short wavelengths of the Chang'E instruments to uniquely constrain the geothermal flux. Longer wavelengths will be required to map the lower heat flux seen over most of the Moon and other bodies, highlighting a path forward in future spacecraft instrumentation. Such data should be ground-truthed on the Moon by a globally distributed heat flux network [13,36]. Techniques such as in-situ heat flux, seismic, electromagnetic, long wavelength radar exploration, and sample geochemical analysis could further characterize the presence, size, and origin of the Compton-Belkovich pluton system. Our results conclude that this is a highly-evolved, multi-stage, batholith-scale, granitic magmatic system – a phenomenon previously documented only on Earth.

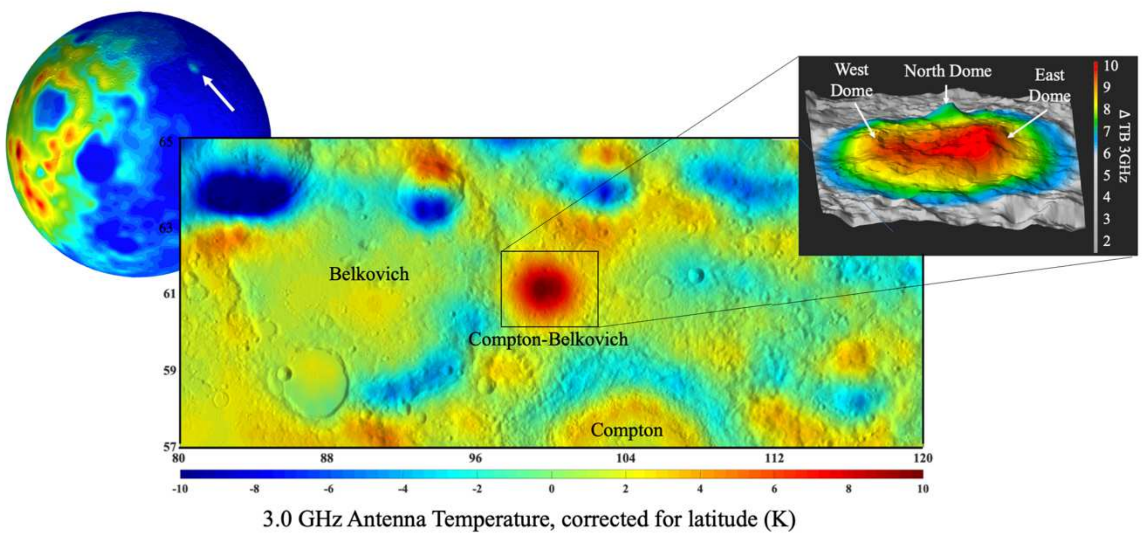

Figure 1: Latitudinally corrected 3 GHz antenna temperature (ΔTA) at midnight local time shows a clear localized enhancement of about 10K centered on the mapped Compton-Belkovich topographic feature. This feature is not explainable by topography, surface rock distribution, or material properties and is seen at all frequencies and times of day (see Methods). The context globe shows Lunar Prospector measured Th. (top left), while the perspective view shows the antenna temperature superimposed on a local topography model (top right).

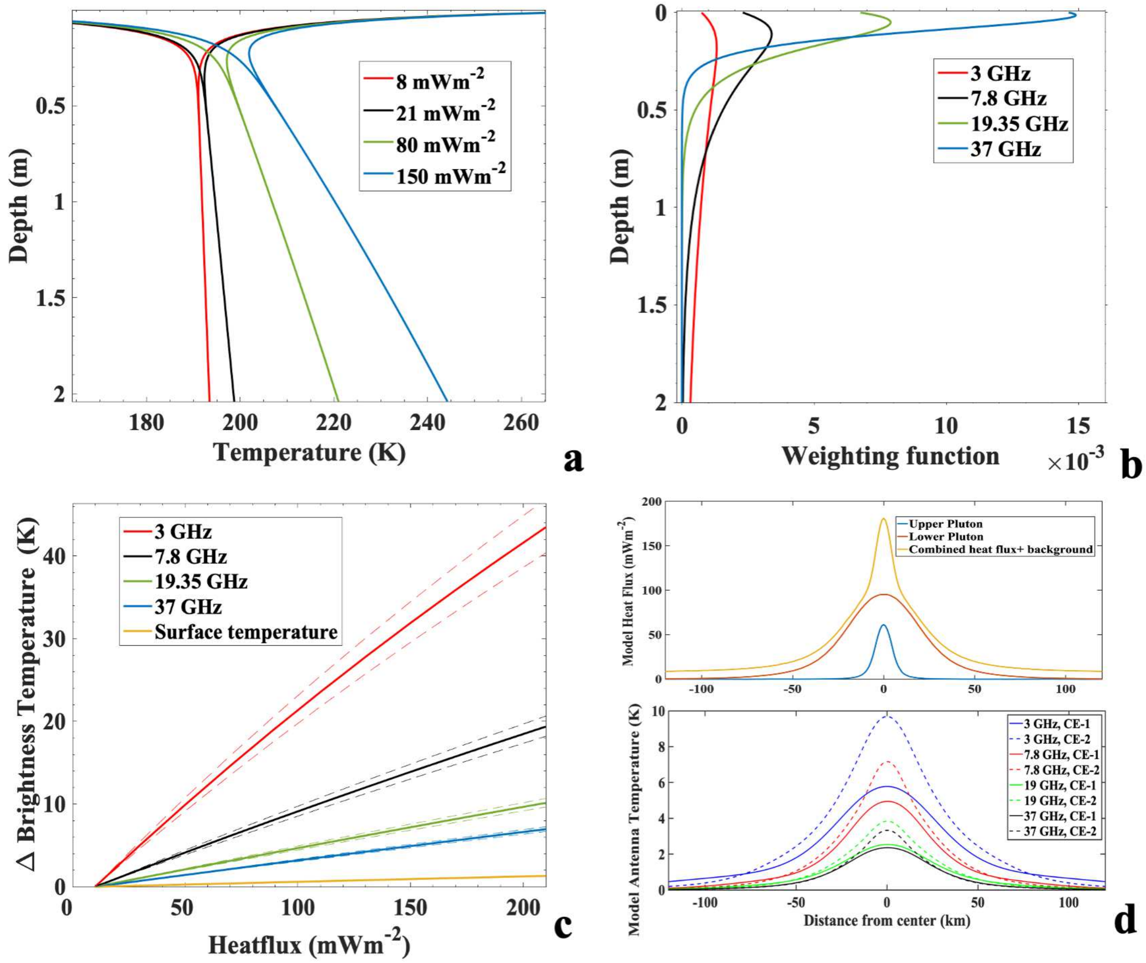

Figure 2: (a) Physical temperature vs depth for C-B location for various geothermal fluxes, (b) CE MRM weighting functions in highlands regolith, (c) Change in brightness temperature for a given heat flux; ±10% in loss tangent in dashed lines, (d) top, heat flux from our nominal two pluton mode (orange) resulting from the combined upper (blue) and lower (red) pluton contributions with 8mWm^{-2} background heat flux; bottom, resulting ΔTA for each measurement for our simplified two pluton model.

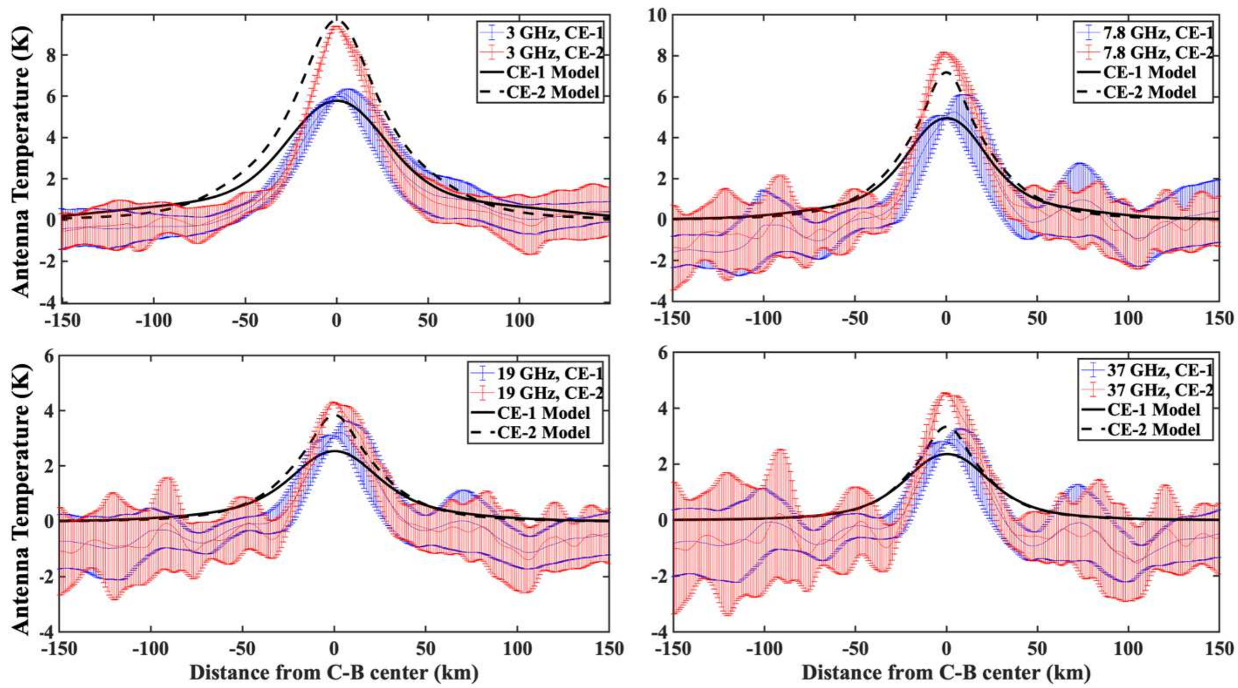

Figure 3: Data minus forward model antenna temperature compared with the best-fit pluton model prediction of the 3-37 GHz Chang'E 1 and 2 data as a function of distance from the center of C-B. Negative values are averages in radial distance from C-B with 1-sigma error for all data westward of the feature; positive for those eastward. A clear spike is seen at all frequencies as mapped in Figure 1 and the Methods. Figure 2d (upper) shows input model heat flux values.

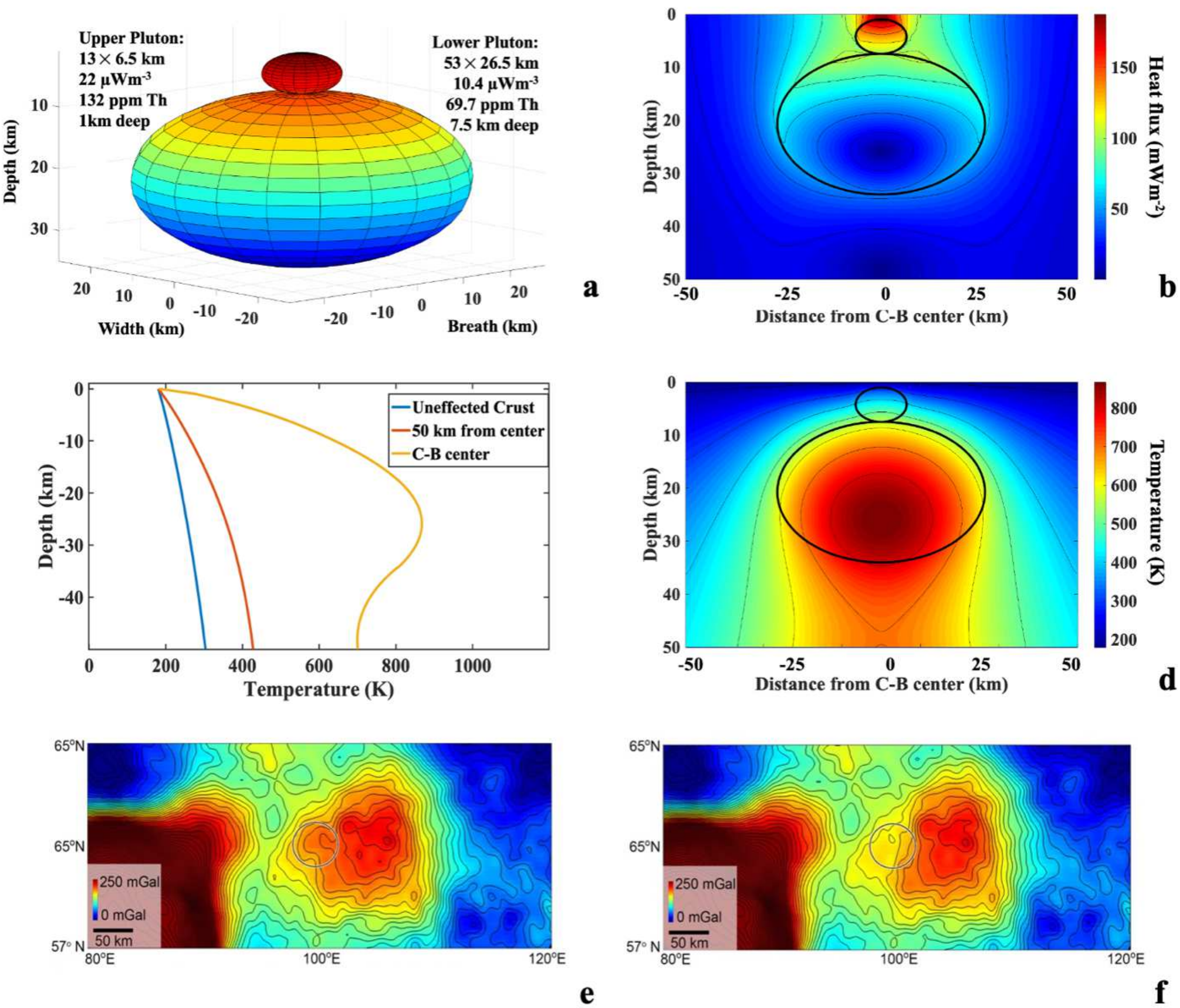

Figure 4: (a) Our favored Compton-Belkovich pluton model based on fitting of the surface heat flux enhancement, (b) the resulting heat flux, and (c-d) subsurface temperatures predicted by this model, (e) GRAIL Bouguer gravity of C-B region, and (f) GRAIL Bouguer gravity after removing the gravity signature of a model from the middle of our preferred range (90 kg/m^3 density anomaly for the lower body). In e and f, the C-B gravity anomaly associated with this pluton sits on the shoulder (small circle) of a broader and higher magnitude anomaly associated with the larger C-B region.

Supplemental Data:

The data used to make all maps in this paper is available online at: https://doi.org/10.5281/zenodo.7058680

The original Chang'E-1 and Chang'E-2 MRM data can be downloaded from: http://moon.bao.ac.cn/index_en.jsp.

Our group (contact Michael St. Clair - mstclair@millionconcepts.com) has also produced a readable global gridded data product of all available Chang'E 1 and Chang'E 2 data at: https://zenodo.org/record/7058552

References:

[1] Pitcher, W. S. *The nature and origin of granite*. Springer Science & Business Media, 1997.

[2] Seddio S.M., Korotev R.L., Jolliff B.L., Wang A.(2015) Silica polymorphs in lunar granite: Implications for granite petrogenesis on the Moon. *American Mineralogist*, 100 (7): 1533–1543. https://doi.org/10.2138/am-2015-5058

[3] Glotch, T. D., Lucey, P. G., Bandfield, J. L., Greenhagen, B. T., Thomas, I. R., Elphic, R. C., ... & Paige, D. A. (2010). Highly silicic compositions on the Moon. *Science*, *329*(5998), 1510-1513.

[4] Lawrence, D. J., Puetter, R. C., Elphic, R. C., Feldman, W. C., Hagerty, J. J., Prettyman, T. H., & Spudis, P. D. (2007). Global spatial deconvolution of Lunar Prospector Th abundances. *Geophysical Research Letters*, *34*(3).

[5] Hagerty, J. J., Lawrence, D. J., Hawke, B. R., Vaniman, D. T., Elphic, R. C., & Feldman, W. C. (2006). Refined thorium abundances for lunar red spots: Implications for evolved, nonmare volcanism on the Moon. *Journal of Geophysical Research: Planets*, *111*(E6).

[6] Wilson, J. T., Eke, V. R., Massey, R. J., Elphic, R. C., Jolliff, B. L., Lawrence, D. J., ... & Teodoro, L. F. A. (2015). Evidence for explosive silicic volcanism on the Moon from the extended distribution of thorium near the Compton-Belkovich Volcanic Complex. *Journal of Geophysical Research: Planets*, *120*(1), 92-108.

[7] Jolliff, B. L., Tran, T. N., Lawrence, S. J., Robinson, M. S., Scholten, F., Oberst, J., ... & Paige, D. A. (2011a, March). Compton-Belkovich: Nonmare, Silicic Volcanism on the Moon's Far Side. In *42nd Annual Lunar and Planetary Science Conference* (No. 1608, p. 2224).

[8] Jolliff, B. L., Wiseman, S. A., Lawrence, S. J., Tran, T. N., Robinson, M. S., Sato, H., ... & Paige, D. A. (2011b). Non-mare silicic volcanism on the lunar farside at Compton–Belkovich. *Nature Geoscience*, *4*(8), 566-571.

[9] Jolliff, B. L., Zanetti, M., Shirley, K. A., Accardo, N. J., Lauber, C., Robinson, M. S., & Greenhagen, B. T. (2012, March). Compton-Belkovich volcanic complex. In *Lunar and Planetary Science Conference* (No. 1659, p. 2097).

[10] Chauhan, M., Bhattacharya, S., Saran, S., Chauhan, P., & Dagar, A. (2015). Compton–Belkovich volcanic complex (CBVC): An ash flow caldera on the Moon. *Icarus*, *253*, 115-129.

[11] Head, J. W., & Wilson, L. (2017). Generation, ascent and eruption of magma on the Moon: New insights into source depths, magma supply, intrusions and effusive/explosive eruptions (Part 2: Predicted emplacement processes and observations). *Icarus*, *283*, 176-223.

[12] del Potro, R., Díez, M., Blundy, J., Camacho, A. G., & Gottsmann, J. (2013). Diapiric ascent of silicic magma beneath the Bolivian Altiplano. *Geophysical Research Letters*, *40*(10), 2044-2048.

[13] Siegler, M.A., Warren, P., Lehman Franco, K., Paige, D.A., Feng, J., White, M.N.(2022) Lunar Heat Flow: Global Predictions and Reduced Heat Flux, JGR Planets, https://doi.org/10.1029/2022JE007182

[14] Wilson, L. and Head, J.W. (2016) Explosive volcanism associated with the silicic Compton-Belkovich volcanic complex: implications for magma water content. 47th Lunar and Planetary Science Conference, 1564

[15] Feng, J., Siegler, M. A., & Hayne, P. O. (2020). New constraints on thermal and dielectric properties of lunar regolith from LRO diviner and CE-2 microwave radiometer. *Journal of Geophysical Research: Planets*, *125*(1), e2019JE006130.

[16] Siegler, M. A., Feng, J., Lucey, P. G., Ghent, R. R., Hayne, P. O., & White, M. N. (2020). Lunar titanium and frequency-dependent microwave loss tangent as constrained by the Chang'E-2 MRM and LRO diviner lunar radiometers. *Journal of Geophysical Research: Planets*, *125*(9), e2020JE006405.

[17] Langseth, M. G., Keihm, S. J., & Peters, K. (1976, April). Revised lunar heat-flow values. In *Lunar and planetary science conference proceedings* (Vol. 7, pp. 3143-3171).

[18] Seddio, S. M., Jolliff, B. L., Korotev, R. L., & Carpenter, P. K. (2014). Thorite in an Apollo 12 granite fragment and age determination using the electron microprobe. *Geochimica et Cosmochimica Acta*, *135*, 307-320.

[19] Wieczorek, M. A., Neumann, G. A., Nimmo, F., Kiefer, W. S., Taylor, G. J., Melosh, H. J., ... & Zuber, M. T. (2013). The crust of the Moon as seen by GRAIL. *Science*, *339*(6120), 671-675.

[20] Siegler, M. A., & Smrekar, S. E. (2014). Lunar heat flow: Regional prospective of the Apollo landing sites. *Journal of Geophysical Research: Planets*, *119*(1), 47-63.

[21] Ryder, G., & Martinez, R. R. (1991). Evolved hypabyssal rocks from station 7, Apennine Front, Apollo 15. In *Proceedings of Lunar and Planetary Science Volume 21*. Lunar and Planetary Institute.

[22] Warren, P. H., Taylor, G. J., & Keil, K. (1983). Regolith breccia Allan Hills A81005: Evidence of lunar origin, and petrography of pristine and nonpristine clasts. *Geophysical Research Letters*, *10*(9), 779-782.

[23] Seddio, S. M., Jolliff, B. L., Korotev, R. L., & Zeigler, R. A. (2013). Petrology and geochemistry of lunar granite 12032, 366-19 and implications for lunar granite petrogenesis. *American Mineralogist*, *98*(10), 1697-1713.

[24] Goossens, S., Sabaka, T. J., Wieczorek, M. A., Neumann, G. A., Mazarico, E., Lemoine, F. G., Nicholas, J.B., Smith,D.E. & Zuber, M. T. (2020). High-resolution gravity field models from GRAIL data and implications for models of the density structure of the Moon's crust. *Journal of Geophysical Research: Planets*, *125*(2), e2019JE006086.

[25] Kiefer, W.S., Macke, R. J., Britt, D. T., Irving, A.J, Consolmagno, G. J. (2012) The density and porosity of lunar rocks. *Geophys. Res. Lett.* **39**, L07201.

[26] Gillis, J. J., et al. "The Compton-Belkovich Region of the Moon: Remotely Sensed Observations and Lunar Sample Association." *Lunar and Planetary Science Conference*. 2002.

[27] Laneuville, M., Wieczorek, M. A., Breuer, D., Aubert, J., Morard, G., & Rückriemen, T. (2014). A long-lived lunar dynamo powered by core crystallization. *Earth and Planetary Science Letters*, *401*, 251-260.

[28] Neal, C. R., & Taylor, L. A. (1989). The nature and barium partitioning between immiscible melts-A comparison of experimental and natural systems with reference to lunar granite petrogenesis. In *Lunar and Planetary Science Conference Proceedings* (Vol. 19, pp. 209-218).

[29] Fagan, T. J., Kashima, D., Wakabayashi, Y., & Suginohara, A. (2014). Case study of magmatic differentiation trends on the Moon based on lunar meteorite Northwest Africa 773 and comparison with Apollo 15 quartz monzodiorite. *Geochimica et Cosmochimica Acta*, *133*, 97-127.

[30] Rutherford, M. J., Hess, P. C., Ryerson, F. J., Campbell, H. W., & Dick, P. A. (1976, April). The chemistry, origin and petrogenetic implications of lunar granite and monzonite. In *Lunar and Planetary Science Conference Proceedings* (Vol. 7, pp. 1723-1740).

[31] Ryder, G., Stoeser, D. B., Marvin, U. B., & Bower, J. F. (1975). Lunar granites with unique ternary feldspars. In *Lunar and Planetary Science Conference Proceedings* (Vol. 6, pp. 435-449).

[32] Hess, P. C., Horzempa, P., & Rutherford, M. J. (1989, March). Fractionation of Apollo 15 KREEP basalts. In *Lunar and Planetary Science Conference* (Vol. 20).

[33] Marvin, U. B., Lindstrom, M. M., Holmberg, B. B., & Martinez, R. R. (1991). New observations on the quartz monzodiorite-granite suite. In *Lunar and Planetary Science Conference Proceedings* (Vol. 21, pp. 119-135).

[34] Gullikson, A. L., Hagerty, J. J., Reid, M. R., Rapp, J. F., & Draper, D. S. (2016). Silicic lunar volcanism: Testing the crustal melting model. *American Mineralogist*, *101*(10), 2312-2321.

[35] Warren, P. H. & Wasson, J. T. (1979). The origin of KREEP. *Reviews of Geophysics*, *17*(1), 73-88.

[36] Taylor, S. R., & McLennan, S. (2009). *Planetary crusts: their composition, origin and evolution* (Vol. 10). Cambridge University Press.

[37] Neal, C. R., Weber, R. C., Banerdt, W. B., Beghein, C., Chi, P., Currie, D., ... & Zacny, K. (2020). The Lunar Geophysical Network (LGN) is critical for solar system science and human exploration.

Methods:

1: Instrument background and Loss Tangent maps

The Microwave RadioMeter (MRM) instruments carried by CE-1 and CE-2 made measurements in four spectral channels (3.0, 7.8, 19.35, and 37 GHz) [38]. The CE-1 data have channel-dependent resolutions of ~35 - 50 km from its orbital altitude of ~200 km, while the CE-2 data have resolutions of ~17.5 - 25 km because its orbital altitude was ~100 km. The microwave observations have been used to estimate regolith thickness [39], dielectric properties [15,16, 40], rock abundance [41,42], subsurface temperatures [43], and geothermal heat flow [44,45] as well as the eruption phase of basaltic volcanism in the Mare of the Moon [46]. In the polar region, MRM data analysis usually focuses on searching for evidence of water ice [47] and studying the thermal gradient [48].

A quantity known as the dielectric loss tangent, *tanδ*, controls the depth from which microwave energy is emitted. This is simply the ratio between the real, *ε'*, and imaginary, *ε"*, dielectric constants, with $\tan\delta = \varepsilon''/\varepsilon'$. **Extended Data Figure 1** shows the mapped "integrated loss tangent," or average loss tangent over the depth sounded by a given frequency as described in Siegler et al. [16]. These maps are based on diurnal microwave amplitudes, increasing with higher loss as soundings are closer to the surface. Diurnal amplitudes are fit using all data within a ¼ degree box of each point. As discussed in Feng et al. [15] and Siegler et al. [16], there appear to be substantial offsets in the absolute temperature calibration of the Chang'E data, but the relative calibration (comparing location to location or diurnal amplitudes) appears robust and in alignment with model expectations. All work in this paper relies on relative calibration (e.g., how hot Compton-Belkovich is compared to its surroundings at a given frequency).

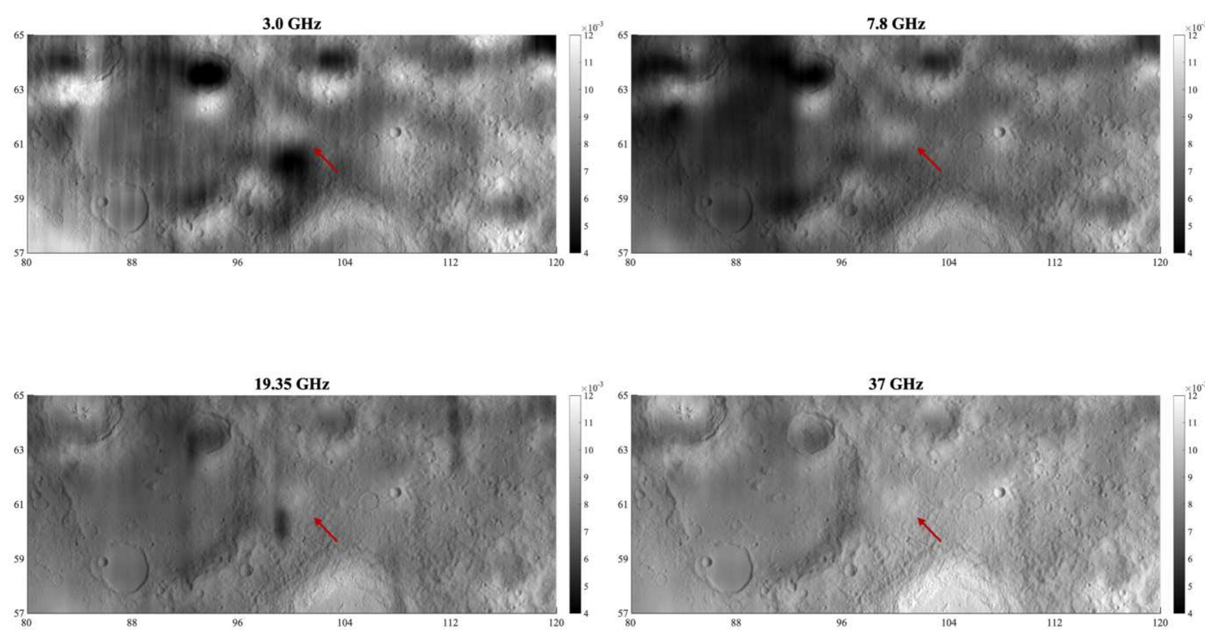

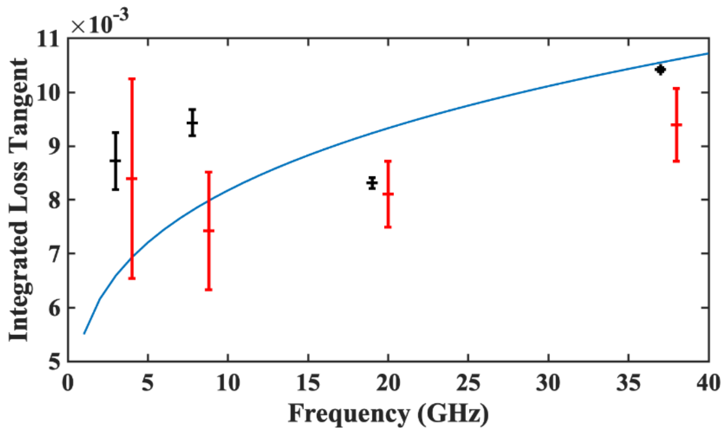

Extended Data Figure 1: (upper) Integrated loss tangent for each of the four frequencies derived from Chang'E 2 microwave amplitudes and thermal model fits (as in [16])(lower) Integrated loss tangent as a function of frequency for (black) the areas within 1 degree of C-B, (red) the entire maps in ED1, and (blue) the highlands terrain model from [16]. The blue line is used for our modeling of the C-B heat flux.

From these maps, we argue that there is no loss anomaly associated with the Compton-Belkovich feature that could explain the enhanced antenna temperature. Features such as Dugan J (the small, fresh crater directly to the East of C-B) or Compton crater (the large crater at ~57 N,104 E) have a higher loss. The apparent low loss areas on high latitude craters result from low amplitudes due to topographic shadowing not accounted for in these fits. **Extended Data Figure 1** illustrates the average integrated loss tangent for C-B (black) and the entire map in **Extended Data Figure 1** (red) as compared to the highlands terrain model from [16] (blue line). However, a high loss would *decrease* the apparent heat flux, not increase it- making our heat flux estimates a lower limit. Overall, the average highlands model (fit to global data) appears justified for use over this entire region. These global fits are likely more reliable than the mapped values in **Extended Data Figure 1** as high latitude (such as C-B at ~61N) fits may be biased by small shadows and surface roughness. The striping in **ED1** is due to variable time of day coverage in producing a fit to the diurnal amplitude.

Based on this, we use the Siegler et al. [16] loss tangent to derive appropriate microwave weighting functions, *w,* which relates the physical temperature vs. depth, *T(z)*, to the microwave brightness temperature at a given frequency as $T_b = \int_0^\infty w(z)T(z)$. In a non-scattering medium with a layered model (for each layer *i*) based on Ulaby *et al.* [49,50], the weighting function, w_i, can be expressed as:

$$w_i = (1 - e^{-\kappa_i d_i}) \cdot (1 + \left|R_{i(i+1)}\right|^2 \cdot e^{-\kappa_i d_i}) \cdot \prod_{j=0}^{i-1} \left(\left[1 - \left|R_{j(j+1)}\right|^2\right] \cdot e^{-\kappa_j d_j}\right) \qquad (1)$$

where κ_i is the power absorption coefficient of layer *i*, d_i is the layer thickness, and $R_{i(i+1)}$ is the reflection coefficient between layer *i* and layer *i+1*. For nadir observations (no off-nadir data is used in this paper), $R_{i(i+1)}$ is given from the real dielectric constant of the layer such that:

$$R_{i(i+1)} = \frac{\sqrt{\varepsilon'_{i+1}} - \sqrt{\varepsilon'_i}}{\sqrt{\varepsilon'_{i+1}} + \sqrt{\varepsilon'_i}} \qquad (2)$$

the power absorption coefficient, κ_i, is given by:

$$\kappa_i = 2\frac{2\pi f}{c}\left(\frac{\varepsilon'}{2}(\sqrt{1 + \tan^2\delta} - 1)\right)^{1/2} \qquad (3)$$

where *f* is the frequency, *c* is the speed of light, *ε'* is the real dielectric constant (which we set as 1.92^{ρ} [51]), and *tanδ* is the loss tangent. κ_i determines the penetration depth of microwave radiation. As physical temperature amplitudes decrease with depth and loss changes the depth being sensed, the diurnal amplitude of T_b can be used to calculate the κ_i and dielectric loss (see details in [15,16]).

2: Antenna Model

Model antenna temperature, *TA*, results from a convolution of the emitted brightness temperature (*Tb*) from the Moon and the instrument antenna pattern. During the ground calibration test for the Chang'E-1 system, the antenna patterns of the four channels were measured [52]. In this study, we fitted the antenna pattern of four channels in a gaussian form based on published parameters. These parameters provided constraints on the main beam and the 3dB efficiency and beamwidth. As the main lobe contributes >68% of the total signal at all frequencies [52], we only consider the main lobe and the first side lobes, which are treated as secondary Gaussians. Chang'E-1 MRM and Chang'E-2 MRM are almost identical, so the same angular antenna radiation pattern is used for both data sets. **Extended Data Figure 2** gives the modeled antenna patterns of four frequencies. For simplicity, we have assumed symmetric antenna patterns, but in reality, there are small differences in the E and H plane beamwidth.

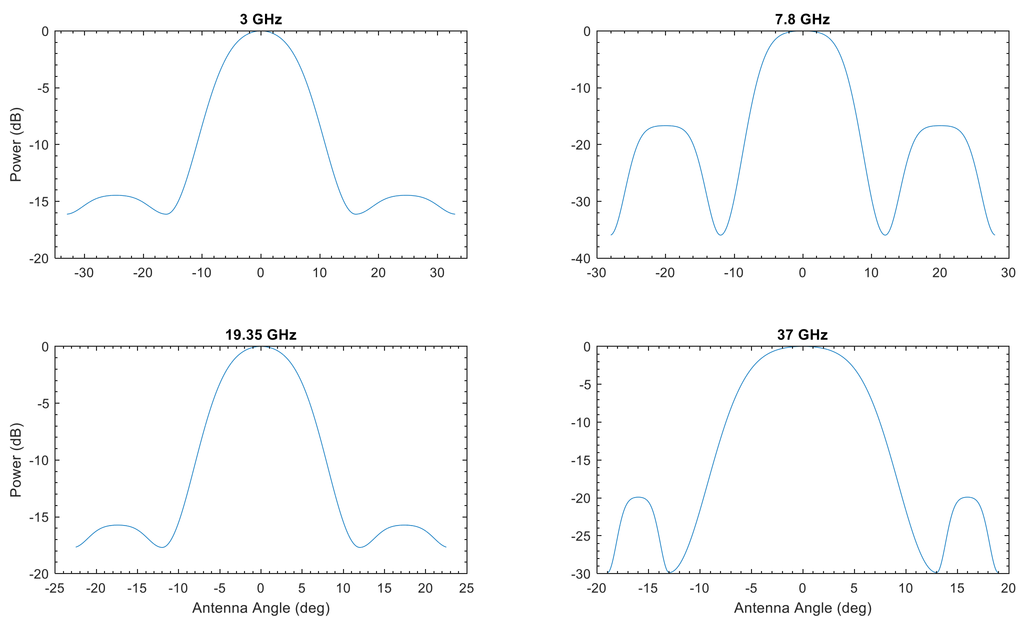

Extended Data Figure 2: Simulated antenna patterns for each of the four MRM frequencies. Here they are plotted in antenna angle, leading to different spatial footprints for the Chang'E 1 vs. 2 missions due to their 200 and 100 km altitudes.

This multi-frequency, multi-altitude fit allows for the constraint of a unique source function of the emitted heat from the surface. These patterns result in a different area in the instrument footprint filled with the C-B heat source at each frequency. For example, the spatial footprint (generally defined by the 3dB values) is approximately 25 km for CE-2 at 3 GHz and 17.5 km for the remaining channels. For CE-1 (approximately at twice the orbital altitude), this is 50 and 35 km, respectively. This will cause a smearing of any heat source that is dependent on frequency and altitude.

As discussed in the following section, we perform some simple processing of the Chang'E data, such as latitude correction. We do not otherwise change the data from the available antenna temperature, *TA*, values in the Chang'E archive (included in supplementary data) for effects such as footprint resolution, but instead process only our forward model of *Tb* to create a model antenna temperature, *TA*. Also, as discussed in the following section, we use our antenna pattern and a thermal model for the C-B region to produce a forward model of the *TA* that should be observed from solar heating alone. We then can subtract this from the data to create a map of *TA* that is ideally solely from increases in geothermal heat. We then produce forward models of geothermal heating from our pluton models (shown in **Extended Data Figure 3**) to produce a map of surface heat flux. Cross sections of our favored model heat flux are shown in **Figure 2D** (upper). We then convert this to a brightness temperature signal including a convolution with the antenna pattern for a given frequency, with the resulting *TA* as shown in **Figure 2D** (lower) and **Figure 3**.

As shown in **Figure 2c**, there is an approximately linear relationship between the brightness temperature and geothermal gradient at any given frequency. For the highlands average loss tangent[16], this relationship follows as (for a heat source, *HF*, in units of Wm^{-2}):

$$Tb\_3G = -89.24 * HF^2 + 166.2 * HF - 1.294$$
$$Tb\_7.8G = -24.23 * HF^2 + 79.14 * HF - 0.6259$$
$$Tb\_19G = -8.118 * HF^2 + 43.94 * HF - 0.3494$$
$$Tb\_37G = -4.520 * HF^2 + 31.17 * HF - 0.2482$$

10% changes in the loss tangent will result in fits plotted as dashed lines in **Figure 2c**. This relationship assumes a background heat flux of 8 mWm^{-2}, which was a reasonable expectation for this region based on the crustal heat production models shown in **Figure 4**.

We then perform some straightforward processing of the Chang'E data itself, such as latitude correction as discussed in the following section. Also as discussed in the following section, we use our antenna pattern and a thermal model for the C-B region to produce a forward model of the *TA* that should be observed from solar heating alone. We then can subtract this from the data to produce a map of *TA* that is ideally solely from increases in geothermal heat. Finally, we plot the *TA* models from geothermal heating (from **Figure 2D**, lower) against the data (corrected for latitude) in **Figure 3**.

3: Data processing

To produce mapped values of microwave brightness temperature, we interpolated the raw data points of MRM measurements into grided data map. This is the same process used in [15] and [16] and produces approximately ¼ degree resolution maps for Chang'E 2 MRM data. These data are shown in a time series in **Extended Data Figure 3a,** which shows that C-B is hotter than the surroundings at all local time at all frequencies**.** These data are shown as a noontime map in **Extended Data Figure 3b**. These maps highlight the C-B hotspot, but it is not necessarily larger than variations due to topography. We then remove topographic effects with models of the effects of solar illumination. Chang'E 1 data will produce a similar map at lower resolution with a less apparent rise at C-B. We should note here that the absolute values of these brightness temperatures are not a clear match to model expectations given the currently available calibration of Chang'E MRM data. This has been noted in many publications and discussed in detail in [15] and [16].

However, relative changes in Tb are well within line of model expectations. The relative, point-to-point data comparison we rely on here (C-B is hotter than the adjacent area) is quite robust.

Taking advantage of the well-calibrated relative brightness temperature variations, or ΔTb, we can have confidence in maps removing average trends for a given latitude/albedo/slope/loss tangent, etc.. The simplest of those corrections is to remove the brightness temperature trend as a function of latitude. **Extended Data Figure 3c** illustrates how this correction alone makes clear the abnormality of the C-B site. This is most apparent in the 3GHz data, showing the largest relative change from a subsurface heat source. Most other features in the region are clearly related to topography, such as crater rims.

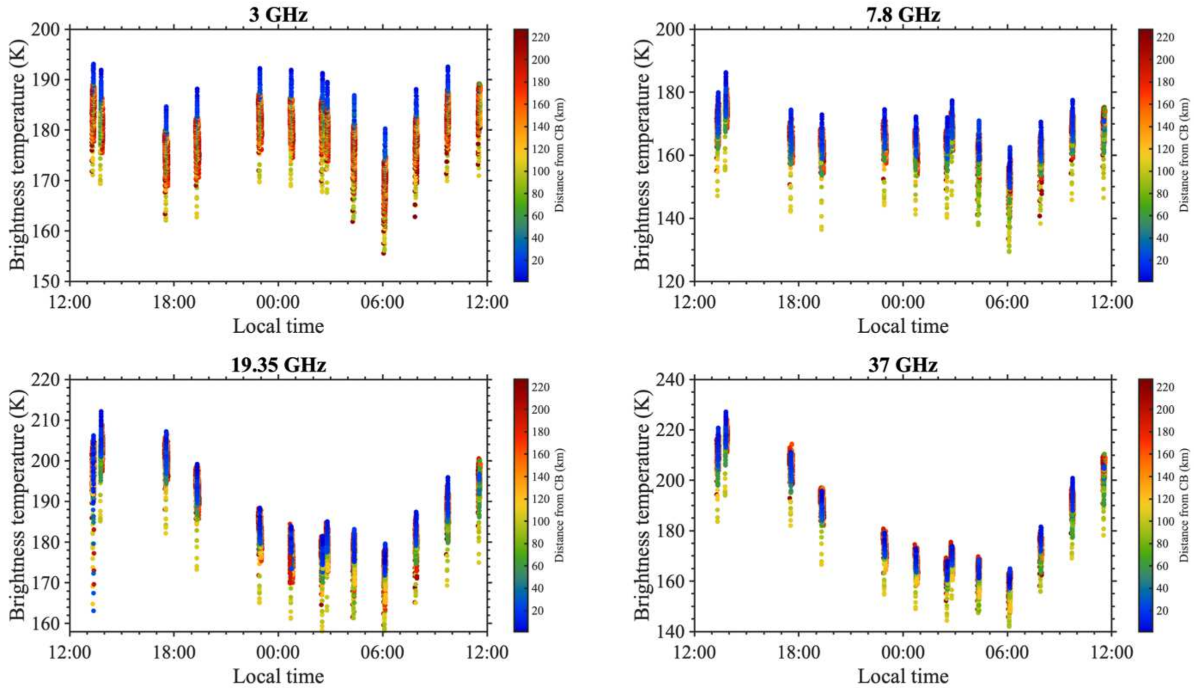

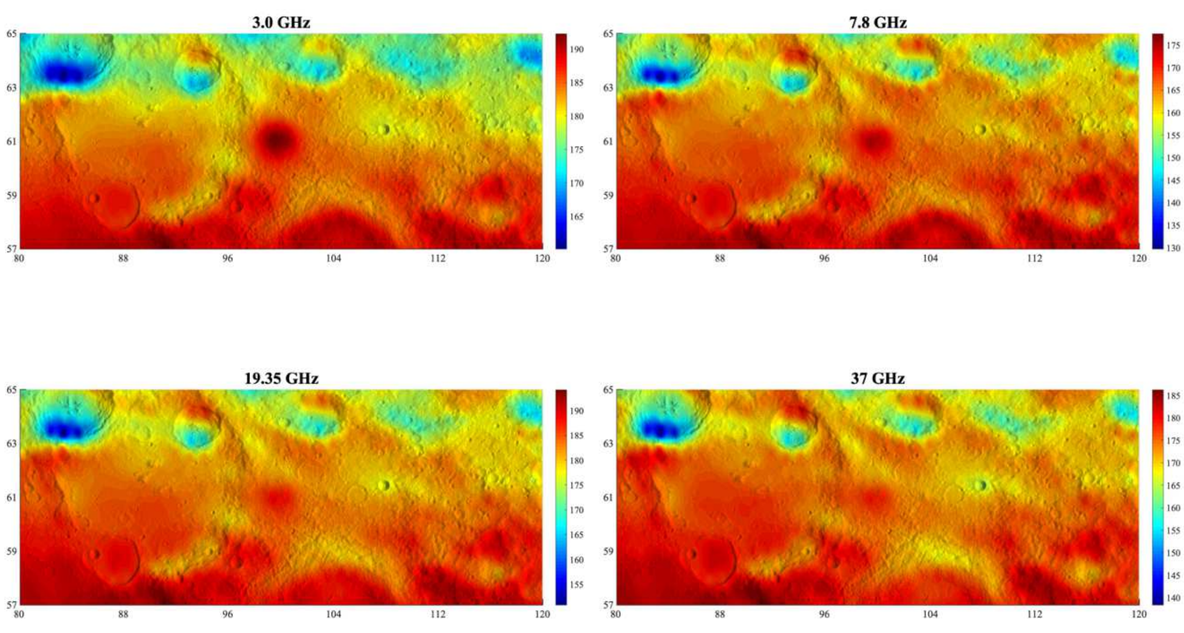

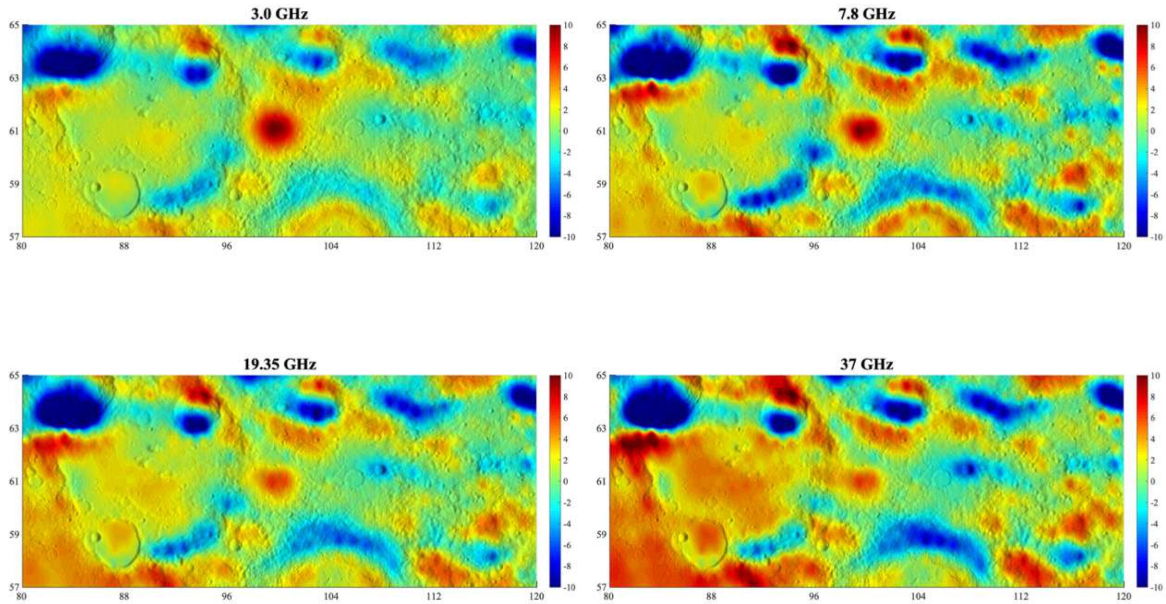

Extended Data Figure 3 (a) Antenna temperatures as a function of time of day and distance from C-B, (b) Gridded noontime antenna temperature data from the Chang'E 2 MRM mission centered at Compton-Belkovich overlain on LROC WAC topography- units in K. (c) Gridded *ΔTA* data from the Chang'E 2 MRM mission centered at Compton-Belkovich after latitude correction overlain on LROC WAC topography- units in K. The 3 GHz 3c figure is used in main text Figure 1.

4: Forward Model of Tb due to solar illumination and topography

To improve upon our ability to fit the Chang'E data with a unique C-B heat flux source, we produce a forward model of expected microwave emission from the region without an anomalous geothermal heat source. We solve the heat diffusion equation for each location at C-B and nearby regions using a standard finite-difference approximation described in [53] to model the lunar surface and subsurface temperature. We include effects of latitude, slope, slope azimuth, rock abundance, albedo, and density profiles (characterized by the scale height of density or H-parameter). We then use available slope, azimuth, density, and albedo data to pick the appropriate temperature from a database of pre-run 1D thermal models. This is not a full 3D model in which facets exchange radiation as the authors used previously for studying polar regions [54-58], but more akin to models presented in [16].

We modeled temperatures based on local slope, x, and azimuth angle, γ (radians from north) computed from the gridded LROC digital elevation model. In the temperature calculations, local time t (lunar h=0 to 24) was adjusted based on the east-west component of the slope:

$$t' = t + \frac{12h}{\pi}\ tan^{-1}(x\ sin\gamma)$$

and latitudes ϕ were adjusted based on the north-south component of the slope,

$$\phi' = \phi + \frac{180°}{\pi}\ tan^{-1}(x\ cos\gamma)$$

The normal bolometric bond albedo quantifies the total solar radiation reflected by the lunar surface. The effective solar flux received by the lunar surface, F_e , can be expressed as: $F_e = (1 - A_\theta)F = (A_0 + (1 - cos^{0.2752}\theta)) \cdot S \cdot cos\varphi$, where θ is the solar incidence angle, S is the solar constant (1361 Wm^{-2}), φ is the latitude, and A_0 is the normal bolometric bond albedo. In this study, we use a uniform best fit albedo of 0.12 for the entire C-B region. If anything, this will overestimate the solar heating contribution from the higher albedo C-B feature - but we treat such effects as negligible.

As the thermal conductivity is density-dependent, in the thermal model, the density of regolith at depth z is described by: $\rho(z) = \rho_d - (\rho_d - \rho_s)e^{-z/H}$, where ρ_s and ρ_d are the bounding densities at the surface and at depths much greater than H (ρ_s = 1100 kg/m^3 and ρ_d = 1800 kg/m^3). The thermal conductivity of lunar regolith used in the thermal model is [59,60]: $K(\rho, T) = K_c(\rho)[1 + \chi(T/350)^3]$, where χ is radiative conductivity parameter and $K_c(\rho)$ denotes the contact conductivity, linearly proportional to density [53,61]: $K_c(\rho) = K_d - (K_d - K_s)\frac{\rho_d - \rho}{\rho_d - \rho_s}$, where K_s and K_d are the contact conductivity values at the surface and at depth.

Diviner rock abundance represents the fraction of a pixel covered by rocks larger than ~1 m in diameter. Fundamentally, rock has higher thermal inertia, so it is warmer at night. The contribution of infrared spectral radiance from rocks is given by

$$I_{\mathrm{rock}}(\lambda, T_{rock}) = \varepsilon \frac{2hc^2}{\lambda^2}\left(e^{\frac{hc}{\lambda k T_{rock}}} - 1\right)^{-1}$$

Where T_{Rock} is the physical temperature of rocks, k is the Boltzmann constant, h is the Planck constant, and c is the speed of light in the medium, ε is emissivity and λ is the wavelength. For each pixel with a rock fraction of *f*, the infrared spectral radiance is:

$$I = (1 - f)I_{\mathrm{regolith}} + fI_{\mathrm{rock}}$$

Then the physical temperature of each pixel is calculated from infrared spectral radiance. By applying the thermal model, each location's surface and subsurface temperature at C-B are calculated with surface and modeled brightness temperature at four frequencies before convolution is shown in **Extended Data Figure 5**.

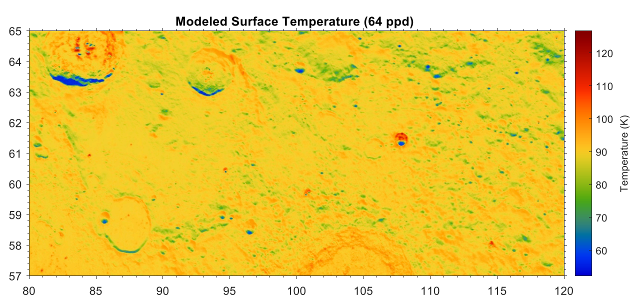

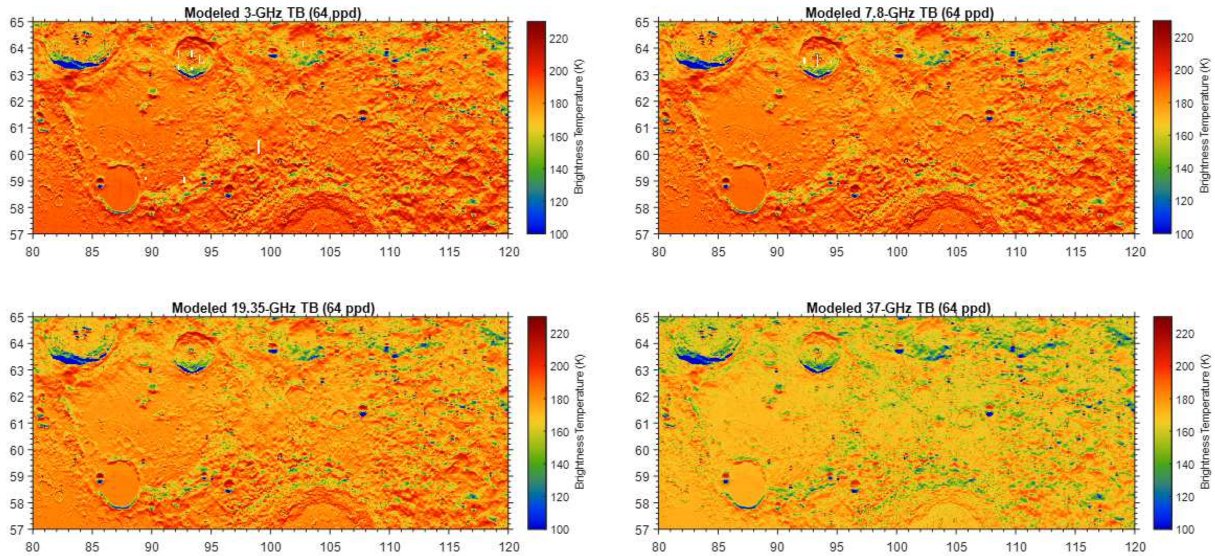

Extended Data Figure 5: (upper) Modeled surface temperature at night without a C-B source. (lower) Full resolution modeled brightness temperature of four frequencies (again without a C-B source) at night before convolution.

The modeled brightness temperatures at four frequencies after convolution with our antenna models are shown in Extended Data Figure 6. As these models do not include reflected radiation, areas like Hayn Crater (North-West corner) are colder than in reality.

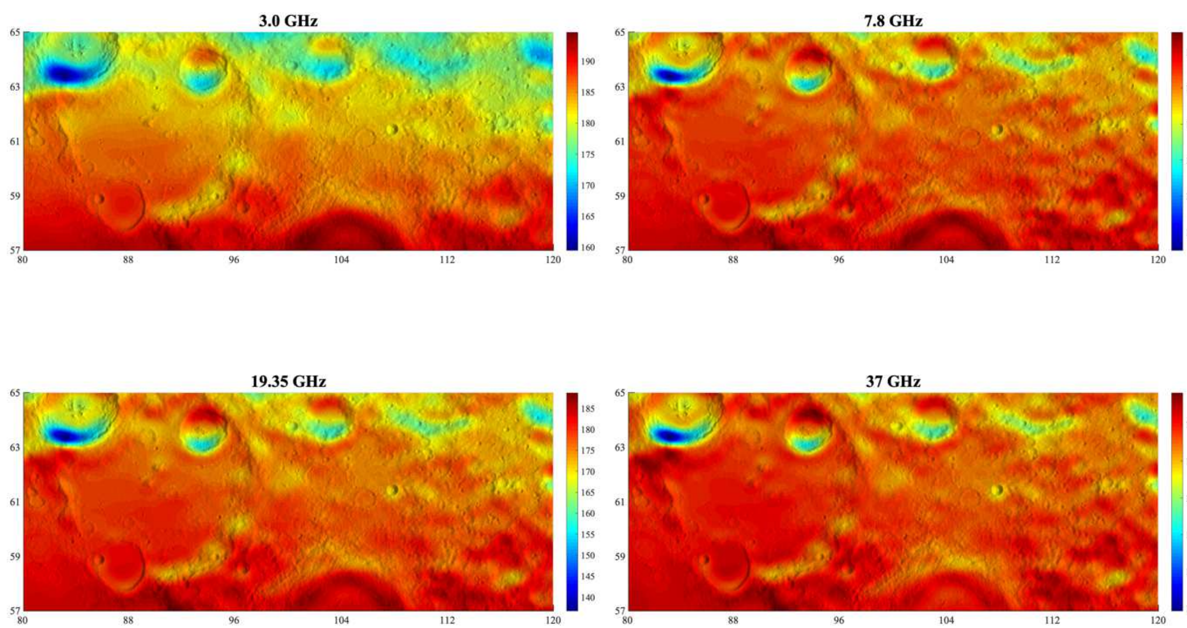

Extended Data Figure 6: The modeled antenna temperature (in the absence of a C-B heat source) at four frequencies after convolution.

This forward model should bear a striking resemblance to **Extended Data Figure 4** if produced properly. This is illustrated in **Extended Data Figure 7**, which shows the data in **ED4** minus the model in **ED6**. While some residuals exist, especially in the high frequency models, most features in the C-B region and ~61° latitude band have been removed. These models are then used to produce **Figure 3**. In that figure, we plot all data in these maps as a function of distance from the center of C-B for convolutions using both the CE-1 and CE-2 orbital altitudes.

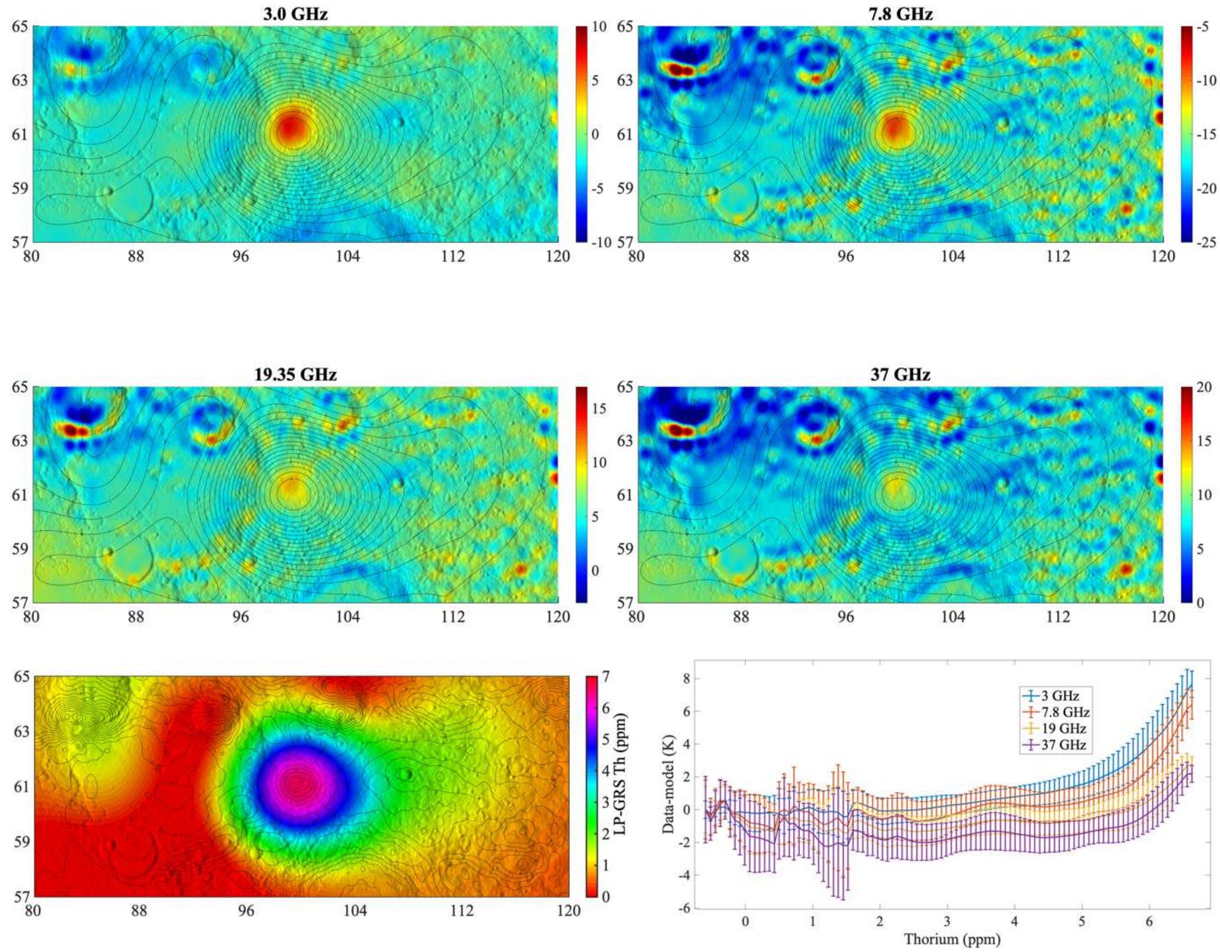

Extended Data Figure 7: (a-d) The "data minus model" residual antenna temperature at four frequencies subtracted from the Chang'E 2 data. Contours map the LP-GRS Th enhancement (after Wilson et al. [6]), (e) The pixon-reconstructed LP-GRS Th concentrations with contours of CE-2 3 GHz data- model values. (f) CE-2 data minus model residual antenna temperature at four frequencies as a function of surface measured Th.

Extended Data Figure 7 also illustrates the coincidence between the microwave brightness temperature enhancement and the derived Lunar Prospector Th enhancement that led to the discovery of Compton-Belkovich [4]. Here we can see a clear spatial correlation between the heat flux anomaly and the LPNS Th, which is also illustrated in **Extended Data Figure 7e**, which shows the inverse picture, with mapped pixon-reconstructed Th values [6] and contours of 3 GHz ΔTB values. However, the directly derived Th concentration (about 7 ppm from the pixon reconstruction, **Extended Data Figure 7e**) is far too low of a radiogenic concentration to explain the ~180 mWm^{-2} heat flux required by our data.

5: Petrologic Parameters

Noting that the surface Th concentrations are too low to explain the heat flux observed at C-B, we use geomorphology and lunar sample petrology to provide reasonable starting points for a heat source model.

The geomorphology of the C-B volcanic complex is consistent with a volcanic caldera [8] that experienced piston-style collapse where the caldera floor faulted downward in a fairly coherent block. This style of collapse forms above ellipsoidal, shallowly emplaced magma chambers [62] whose depth is less than the horizontal dimension [63]. Using the vents within the ring faults as means to constrain the structural diameter of the caldera [10], the magma chamber is predicted to be ~13 km in diameter, likely being composed of smaller bodies, but having the net effect of a single heat source. Petrologic modeling of lunar granites constrains the upper magma emplacement depth to approximately ~1 km [2,34]. These parameters guide our preferred model, which assumes a simplified 2:1 ellipsoid 13 km in diameter (6.5 km thick) and a larger chamber below.

Three generalized granite families found in the Apollo returned sample collection can serve as reasonable estimates of the range of compositions that may exist on the Moon. As noted, the data presented here strongly support a scenario of partial melting and differentiation of KREEP-rich rocks. Indeed, while the deeper emplaced pluton is less enriched in radiogenic elements (~60 ppm Th) than the upper, smaller pluton (~132 ppm Th), this body still has Th concentrations much higher than the Apollo KREEP basalt samples. The enrichment from Apollo KREEP basalt concentrations to those of the modeled lower body are consistent with a partial melting/fractionation evolution that would achieve quartz monzodiorite to granite compositions. Thus, the lower body could form from extensive crystal fractionation of a KREEP basalt parent melt or as a result of partial melting of a KREEP-enriched monzogabbro or alkali gabbronorite lower crust. Likely, an ellipsoidal lower body simplifies a complex magmatic architecture (**Extended Figure 8**).

The presence of a more evolved upper body suggests a multi-stage process wherein more evolved melts were extracted and segregated effectively from the lower magma chamber. Repeated extraction and further crystal fractionation of incompatible element-enriched silicic magmas would enable the formation of the upper magma chamber.

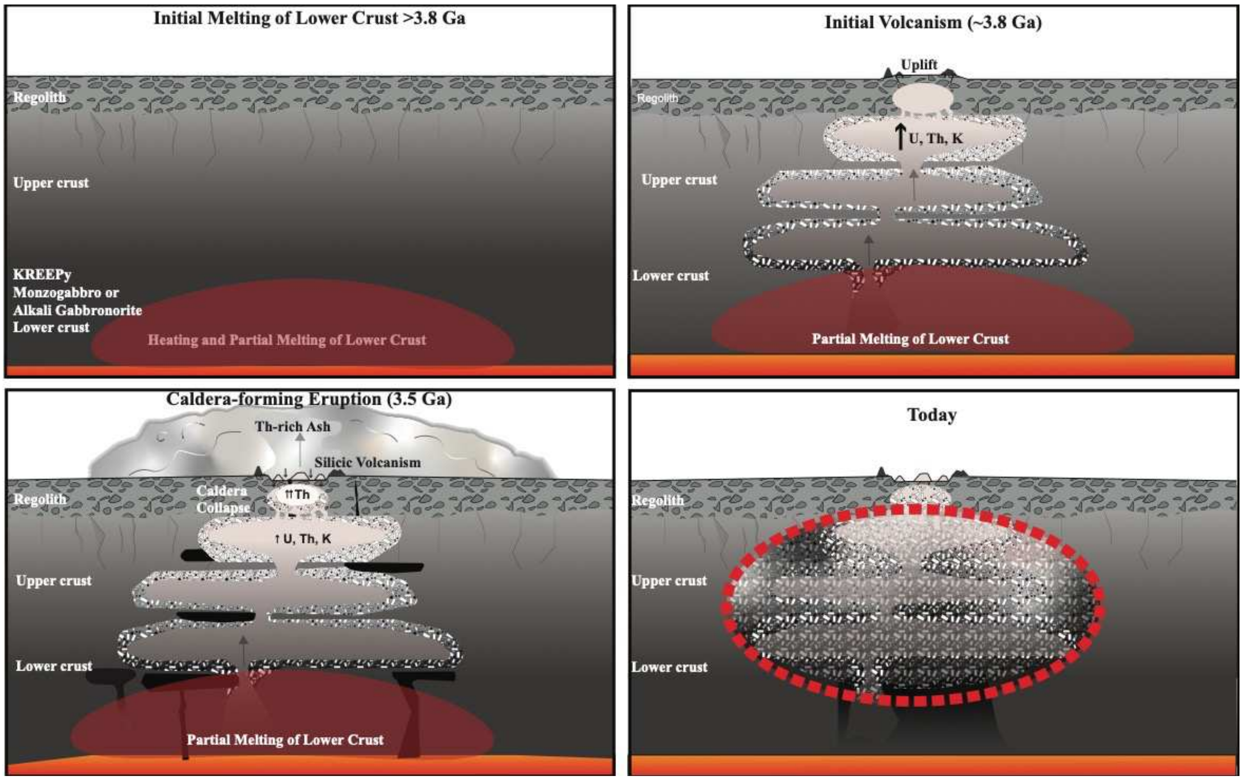

Extended Data Figure 8: The resolution of the gravity and heat flow models is insufficient to inform internal variations in a body that must have formed from a complex system of magma chambers. This figure is one example of a system that could be represented by the Compton Belkovich batholith model and how that system could develop over time.

6: Details of finite element forward models

Our favored model of the 13 km diameter upper pluton and 53km lower pluton is not a unique solution, but is based on patterns seen in 528 example model runs. These steady-state models were produced using a Comsol Multiphysics finite element heat conduction model to enable changes in density and properties as a function of depth. A steady state should be a safe assumption as the last eruptions of C-B were likely >3.5 Gya [64]. We approached the models with fixed parameters designed to minimize the size of both heat-producing bodies. These include:

1) Foremost, we fixed the radiogenic heat production of both bodies. The upper pluton is limited to a heat production of 22 μWm^{-3}, consistent with the highest Th concentration granite found in the lunar sample collection, described here as type G_C. While it may be true that C-B has an even higher concentration of radiogenic materials, we did not think it was reasonable to go beyond this measured value. The lower pluton was then fixed at 10.4 μWm^{-3} heat production, consistent with many moderate Th concentration granites, or type G_B.
2) We forced the bodies to be as close to the surface as we felt plausible. The upper pluton was required to be at 1km depth with the nominal. However, it is a somewhat arbitrary idea that this overburden is needed to have prevented the entire pluton from erupting 3.5

Gya. Moving the upper pluton closer to the surface would not increase heat flux dramatically, mainly affecting the width of the peak well below MRM spatial resolution. We put the lower pluton as near the surface as possible, so it was always just touching the bottom of the upper pluton. The lower pluton can be placed deeper, but this would require the lower pluton to be larger to produce the same surface heat flux and result in a spatially wider signal than seen.

3) We forced the bodies to be ellipsoids, circular in the x-y plane, with a 2:1 aspect ratio. Again, this need not be the case, but this shape is a reasonable first-order model. We note that the horizontal dimensions of the bodies is constrained by the spatial pattern of the *Tb* anomaly, but there will be a tradeoff between the best-fit vertical dimension (or aspect ratio) and assumed heat production.

We approached fitting the models to the data by running a suite of 176 diameter combinations of the two bodies. The upper body was allowed to vary between 10 and 20 km in diameter, with limits set by the geometry of the surface topographic feature. We altered the lower body between 45 and 60 km in diameter. These 176 models were run with three different density profiles and related thermal conductivity using the nominal density/conductivity profiles discussed in [65]. These assume an exponential density profile that increases density by a factor of *e* over a scale height of 1, 5, and 10 km, consistent with GRAIL analysis [66]. The granites were given a thermal conductivity of 3.1 $Wm^{-1}K^{-1}$ [67]. Here density of the granite bodies is set to 2550 kgm^{-3}.

Extended Data Figure 9a illustrates the suite of model fits run to fit the data following the three criteria listed above. These fits consider only the peak heat production with the plotted value representing the absolute value difference between the peak value in the data vs. that of the model. These plots are for the 5 km e-folding model, but show similar results to other models (with best fits noted by *s). The upper plots show the sum of the misfit between the peak in data and model for all four frequencies (for Chang'E 1 and 2, respectively). The lower plots omit 37 GHz data from this fit, as it was most prone to the effects of surface temperature errors in the model.

All the plots show that a narrow avenue of pluton models minimizes the data-model differences. The minimum data-model difference for each crustal density model is plotted as a colored asterisk, though many values along the minimum avenue are notably similar. CE-2 data show a greater tendency towards smaller lower pluton models for large upper plutons due to the fact its lower altitude shows less lateral smearing. Based on surface faulting, we again favor a smaller upper pluton source, leading us towards this range, where all fits favor a roughly 53-56 km wide lower pluton.

Extended Data Figure 9b plots consider the best fit over the area ±15 km around the center of C-B, again for the 5 km e-folding model. Here we again sum the difference between data and model (differencing the lines in **Figure 3**) over all frequencies, hoping to capture more information on the fit to the overall shape of the enhanced brightness temperature. These fits result in a slightly wider "best-fit avenue" with minimum ranges for the lower pluton now centering around 52-55 km diameter. We do not plot minimum values here as they often ended up with a 20 km upper body diameter, which is hard to reconcile with the surface caldera geometry. While it is not unreasonable that a magma source body presently fills a different geometry than our chosen preferred 13 km diameter/6.5 km thickness upper pluton, we use that as a guide for our favored 13 km/53 km upper/lower body geometry.

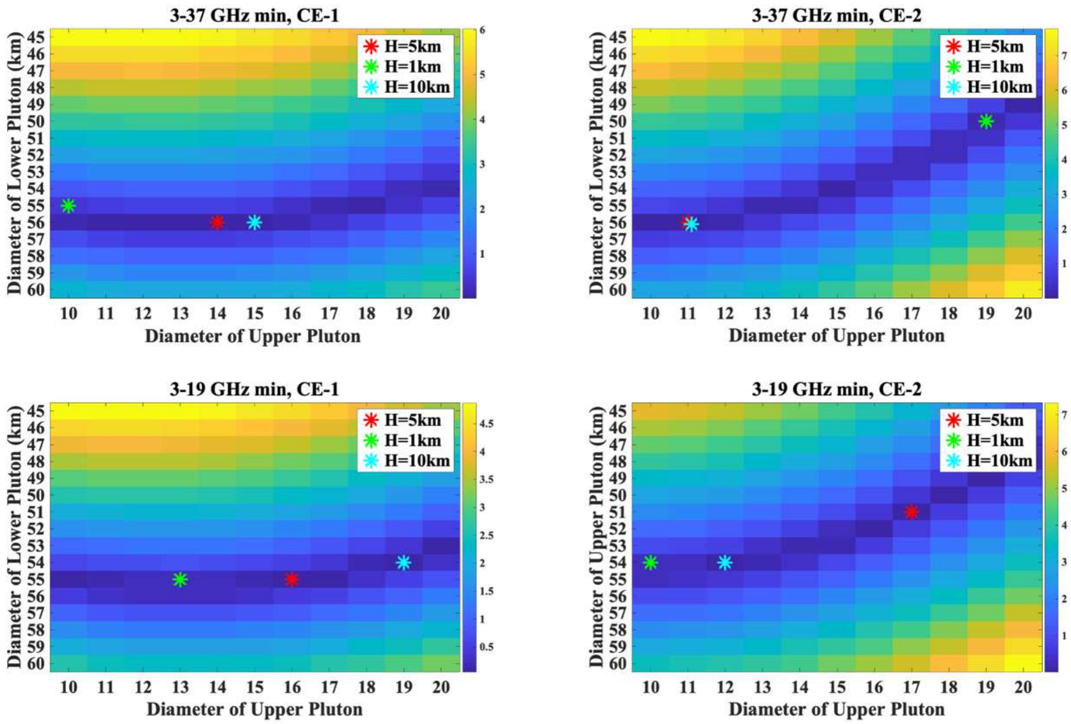

a

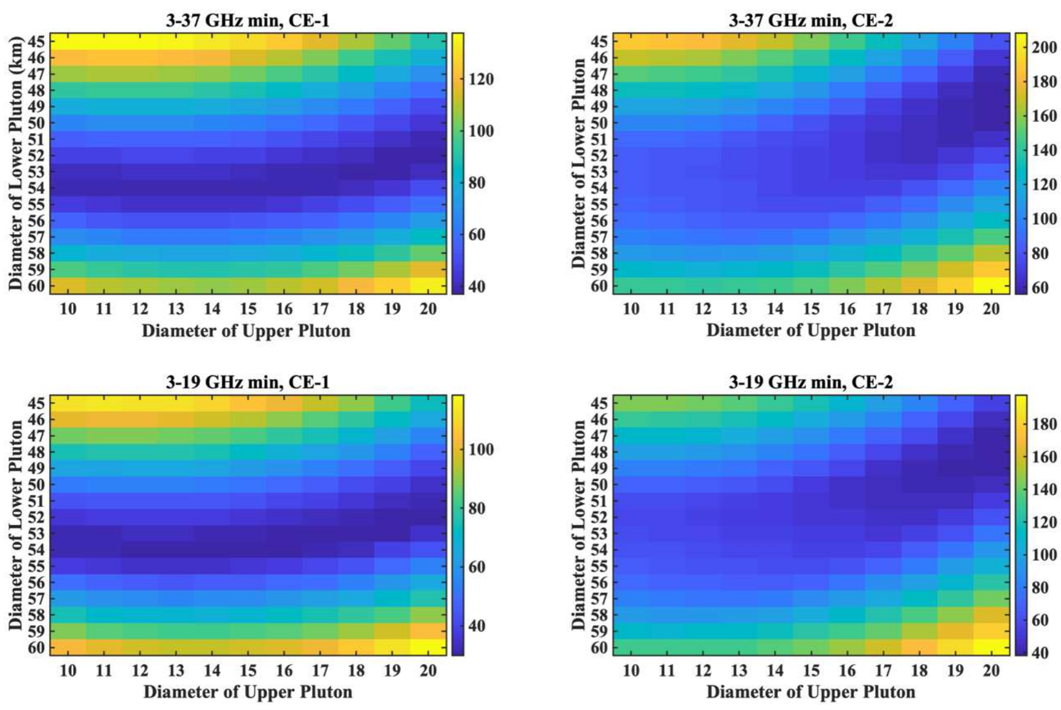

b

Extended Data Figure 9: (a)Absolute data-model differences in peak *TA* for the 5 km e-folding density crustal model for various pluton diameters. (b) Absolute data-model differences in peak *TA* over the area within 15 km of the center of C-B for the 5km e-folding density crustal model for various pluton diameters.

7. Gravity analyses

We took gravity data from the GRGM1200 gravity model [68]. While the rank-minus-one constrained fields of that study provide improved correlations between the free air gravity and topography out to degree 1200, we find that the resulting Bouguer gravity models show orbit parallel striping and other noise beyond degree 500 in this region, and so we limit our analyses to a degree 500 representation of the field. The gravity from topography was calculated [69] assuming a density of 2500 kg/m^3 [19,68] to calculate the Bouguer gravity.

As noted in the main text, the Bouguer gravity shows a distinctive positive gravity anomaly centered on the Th-rich spot and microwave brightness temperature anomaly at C-B. However, this location also exhibits a positive topography mound, consistent with either a volcanic construct or upwarping of the crust above an intrusive body [8]. This raises the possibility that the observed positive Bouguer gravity anomaly at this location is simply a result of an incorrect density assumed in the terrain correction. We find that an assumed crustal density of 3300 kg/m^3 minimizes C-B's distinctive positive gravity anomaly. However, such a high density is at the high end of mare sample densities [70], is greater than regional mare surface densities as constrained by gravity [68], and is incompatible with the inferred silicic surface composition based on Diviner data [8]. A silicic volcanic construct is more likely to have a density similar to the 2500 kg/m^3 value assumed for the surrounding lunar terrain [71].

Although the data shows a distinctive positive gravity anomaly associated with C-B, it is superposed on the shoulder of the broader and larger magnitude Bouguer gravity high associated with a large depression, consistent with either isostatically compensated thinned crust [19] or increased density and decreased porosity due to a regional thermal anomaly [72]. Given the small magnitude of the C-B anomaly relative to this broader gravity high, it is not possible to uniquely constrain the density structure of C-B or directly invert the gravity for the subsurface density structure. Moreover, without added constraints on the geometry or density of the subsurface body, a unique solution is not possible.

Instead, we test whether the favored pluton model is consistent with the observed gravity. We forward-model the gravity arising from the pair of elliptical plutons, decomposing each pluton into a large number of rectangular prismatic elements [73], with a horizontal resolution of 1 km and vertical resolution of 0.5 km. In preliminary tests, we find that the shallow smaller body alone generates an overly sharp gravity anomaly inconsistent with the data. In comparison, the larger deeper body produces a gravity anomaly commensurate with the observations. The favored pluton model indicates a higher Th concentration in the upper body, which would likely be associated with a more evolved and more silicic composition, and, thus a lower density. We impose the constraint that the upper body has a density contrast that is half that of the lower body, and then forward-model the gravity arising from both plutons, which is then subtracted from the data.

We find that density contrasts for the lower body in the range of 60–120 kg/m^3 generate models that, when subtracted from the data, largely remove the small-scale C-B gravity anomaly, leaving behind a smoother shoulder of the broader Compton-Belkovich feature (**Extended data Figure 10**). Larger density contrasts leave behind a negative anomaly at C-B, while smaller density contrasts do not adequately remove the C-B gravity anomaly. The density contrast of the lower body of 60-120 kg/m^3 at a depth of 20.5 km would equate to a density of 2940-3000 kg/m^3, based on a linear density model for the farside highlands [68]. Assuming a low porosity, this density implies a somewhat less dense body than a typical mare [70], suggesting a more silicic composition. The upper body has a smaller density contrast relative to the less dense shallow crust, equivalent to a density of 2470-2500 kg/m^3. This low density is consistent with a more evolved granitic pluton, as inferred based on the microwave data.

We emphasize that the gravity models are not unique, given the variability of the field in this region and the inherent non-uniqueness of potential field data. However, given the preferred pluton structure and the observed gravity anomaly, the conclusion that the lower intrusive body must have a modest positive density contrast while the upper intrusive body must have a weaker density contrast is robust. The upper body thus requires a low absolute density given the vertical density structure of the crust derived from GRAIL gravity data. The resulting density models are consistent with the interpretations based on the microwave data.

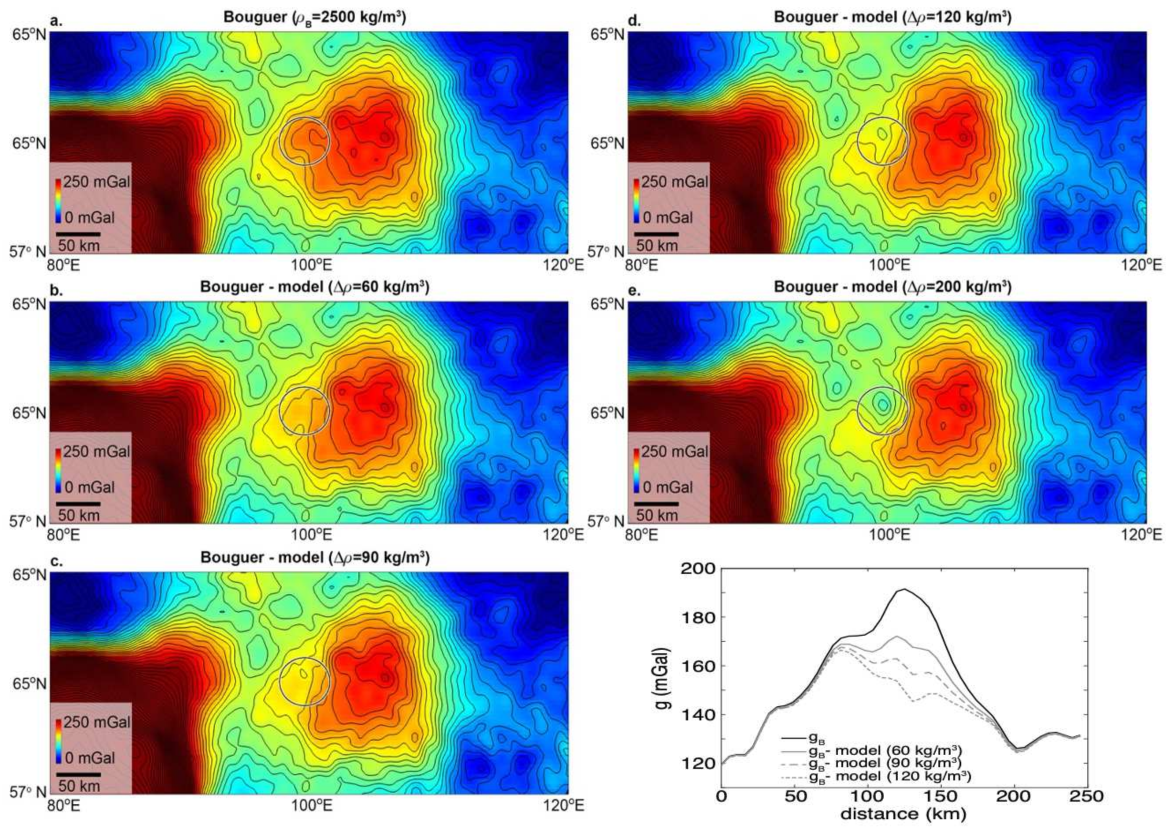

Extended Data Figure 11. Observed Bouguer gravity data and model corrected Bouguer gravity. Bouguer gravity for an assumed crustal density of 2500 kg/m^3, with corrections for the modeled density assuming lower intrusion densities of 60 kg/m^3, 90 kg/m^3, 120 kg/m^3, and 200 kg/m^3. (lower right) North-south profiles of the observed and model corrected Bouguer gravity for assumed density contrasts of 60-120 kg/m^3.

References in Methods

[38] Zheng, Y. et al. (2012) First microwave map of the Moon with Chang'E-1 data: The role of local time in global imaging. Icarus 219, 194-210.

[39] Fa, W. & Jin, Y.-Q. (2010) A primary analysis of microwave brightness temperature of lunar surface from Chang-E 1 multi-channel radiometer observation and inversion of regolith layer thickness. Icarus 207, 605-615.

[40] Gong, X., Paige, D. A., Siegler, M. A. & Jin, Y.-Q. (2014) Inversion of dielectric properties of the lunar regolith media with temperature profiles using Chang'e microwave radiometer observations. IEEE Geosci Remote S 12, 384-388.

[41] Hu, G.-P., Chan, K. L., Zheng, Y.-C., Xu, A.-A. (2018) A Rock Model for the Cold and Hot Spots in the Chang'E Microwave Brightness Temperature Map. IEEE Transactions on Geoscience and Remote Sensing 56, 5471-5480.

[42] Wei, G., Byrne, S., Li, X. & Hu, G. (2020) Lunar Surface and Buried Rock Abundance Retrieved from Chang'E-2 Microwave and Diviner Data. The Planetary Science Journal 1, 56.

[43] Wei, G., Li, X. & Wang, S. (2016) Inversions of subsurface temperature and thermal diffusivity on the Moon based on high frequency of Chang'E-1 microwave radiometer data. Icarus 275, 97-106.

[44] Siegler, M. & Feng, J. (2017) Microwave remote sensing of lunar subsurface temperatures: reconciling Chang'E MRM and LRO diviner. LPI, 1705.

[45] Fang, T. & Fa, W. (2014) High frequency thermal emission from the lunar surface and near surface temperature of the Moon from Chang'E-2 microwave radiometer. Icarus 232, 34-53.

[46] Meng, Z. et al. (2018) Passive microwave probing mare basalts in mare Imbrium using CE-2 CELMS data. Ieee J-Stars 11, 3097-3104.

[47] Wei, G., Li, X. & Wang, S. (2016) Thermal behavior of regolith at cold traps on the moonʹ s south pole: Revealed by Changʹ E-2 microwave radiometer data. Planetary and Space Science 122, 101-109.

[48] Feng, J. & Siegler, M. A. (2021) Reconciling the Infrared and Microwave observations of the lunar South Pole: A study on subsurface temperature and regolith density. Journal of Geophysical Research: Planets 126, e2020JE006623, doi:10.1029/2020JE006623.

[49] Ulaby, F. T., Moore, R. K., & Fung, A. K. (1982). Microwave remote sensing: Active and passive. Volume 2-Radar remote sensing and surface scattering and emission theory.

[50] Ulaby, F. T., Moore, R. K., & Fung, A. K. (1986). Microwave remote sensing: Active and passive. Volume 3-From theory to applications.

[51] Carrier III, W. D., Olhoeft, G. R., & Mendell, W. (1991). Physical properties of the lunar surface. *Lunar sourcebook*, 475-594.

[52] Wang, Z., Li, Y., Zhang, X., JingShan, J., Xu, C., Zhang, D., & Zhang, W. (2010). Calibration and brightness temperature algorithm of CE-1 Lunar Microwave Sounder (CELMS). *Science China Earth Sciences*, *53*(9), 1392-1406.

[53] Hayne, P. O., Bandfield, J. L., Siegler, M. A., Vasavada, A. R., Ghent, R. R., Williams, J. P., ... & Paige, D. A. (2017). Global regolith thermophysical properties of the Moon from the Diviner Lunar Radiometer Experiment. *Journal of Geophysical Research: Planets*, *122*(12), 2371-2400.

[54] Paige, D. A., Siegler, M. A., Harmon, J. K., Neumann, G. A., Mazarico, E. M., Smith, D. E., ... & Solomon, S. C. (2013). Thermal stability of volatiles in the north polar region of Mercury. *Science*, *339*(6117), 300-303.

[55] Paige, D. A., Siegler, M. A., Zhang, J. A., Hayne, P. O., Foote, E. J., Bennett, K. A., ... & Lucey, P. G. (2010). Diviner lunar radiometer observations of cold traps in the Moon's south polar region. *science*, *330*(6003), 479-482.

[56] Siegler, M., Paige, D., Williams, J. P., & Bills, B. (2015). Evolution of lunar polar ice stability. *Icarus*, *255*, 78-87.

[57] Siegler, M. A., Miller, R. S., Keane, J. T., Laneuville, M., Paige, D. A., Matsuyama, I., ... & Poston, M. J. (2016). Lunar true polar wander inferred from polar hydrogen. *Nature*, *531*(7595), 480-484.

[58] Feng, J., & Siegler, M. A. (2021). Reconciling the Infrared and Microwave observations of the lunar South Pole: A study on subsurface temperature and regolith density. *Journal of Geophysical Research: Planets*, *126*(9), e2020JE006623.

[59] Mitchell, D. L., & De Pater, I. (1994). Microwave imaging of Mercury's thermal emission at wavelengths from 0.3 to 20.5 cm. *Icarus*, *110*(1), 2-32.

[60] Whipple, F. L. (1950). The theory of micro-meteorites: Part I. In an isothermal atmosphere. *Proceedings of the National Academy of Sciences*, *36*(12), 687-695.

[61] Vasavada, A. R., Bandfield, J. L., Greenhagen, B. T., Hayne, P. O., Siegler, M. A., Williams, J. P., & Paige, D. A. (2012). Lunar equatorial surface temperatures and regolith properties from the Diviner Lunar Radiometer Experiment. *Journal of Geophysical Research: Planets*, *117*(E12).

[62] Gudmundsson, A. (2008). Magma-chamber geometry, fluid transport, local stresses and rock behaviour during collapse caldera formation. *Developments in Volcanology*, *10*, 313-349.

[63] Geyer, A., Folch, A., & Martí, J. (2006). Relationship between caldera collapse and magma chamber withdrawal: an experimental approach. *Journal of Volcanology and Geothermal Research*, *157*(4), 375-386.

[64] Shirley, K. A., Zanetti, M., Jolliff, B. L., van der Bogert, C. H., & Hiesinger, H. (2012, March). Crater size-frequency distribution measurements at the Compton-Belkovich volcanic complex. In *Lunar and Planetary Science Conference* (No. 1659, p. 2792).

[65] Siegler, M. A., & Smrekar, S. E. (2014). Lunar heat flow: Regional prospective of the Apollo landing sites. *Journal of Geophysical Research: Planets*, *119*(1), 47-63.

[66] Besserer, J., Nimmo, F., Wieczorek, M. A., Weber, R. C., Kiefer, W. S., McGovern, P. J., ... & Zuber, M. T. (2014). GRAIL gravity constraints on the vertical and lateral density structure of the lunar crust. *Geophysical Research Letters*, *41*(16), 5771-5777.

[67] Cho, W. J., Kwon, S., & Choi, J. W. (2009). The thermal conductivity for granite with various water contents. *Engineering geology*, *107*(3-4), 167-171.

[68] Goossens, S., Sabaka, T. J., Wieczorek, M. A., Neumann, G. A., Mazarico, E., Lemoine, F. G., ... & Zuber, M. T. (2020). High-resolution gravity field models from GRAIL data and implications for models of the density structure of the Moon's crust. *Journal of Geophysical Research: Planets*, *125*(2), e2019JE006086.

[69] Wieczorek M. A., Phillips, R. J. (1998), Potential anomalies on a sphere: Applications to the thickness of the lunar crust. *J. Geophys. Res.* 103, 1715–1724.

[70] Kiefer, W. S., Macke, R. J., Britt, D. T., Irving, A. J., & Consolmagno, G. J. (2012). The density and porosity of lunar rocks. *Geophysical Research Letters*, *39*(7).

[71] Kiefer, W. S., G. J. Taylor, J. C. Andrews-hanna, J. W. Head, J. C. Jansen, J. Patrick, K. L. Robinson, M. A. Wieczorek, and M. T. Zuber (2016), The Bulk Density of the Small Lunar Volcanos Gruithuisen Delta and Hansteen Alpha : Implications for Volcano Composition and Petrogenesis, *Lunar Planet. Sci. Conf.*, *47*, Abstract 1722.

[72] Jansen, J. C., Andrews-Hanna, J. C., Li, Y., Besserer, J., Goossens, S., Head, J. W., ... & Zuber, M. T. (2015, March). The Subsurface Structure of the Compton-Belkovich Thorium Anomaly as Revealed by GRAIL. In *Lunar and Planetary Science Conference* (No. 1832, p. 2185).

[73] Blakely, R.J. (1986) Approximating edges of source bodies from magnetic or gravity anomalies. *Geophysics*. 51, 1494–1498.

Author Contributions:

Matthew A. Siegler: Primary writing, central ideas and concepts, figures and funding
Jianqing Feng: Data processing, writing, central ideas and data interpretation
Katelyn Lehman-Franco: Petrologic model synthesis, writing, figure creation
Jeffery C. Andrews-Hanna: Gravity modeling, synthesis, writing
Rita C. Economos: Petrologic model synthesis, writing, advised Lehman-Franco
Michael St. Clair: Lead data product production (of global maps), science discussions, detailed review, editing
Chase Million: Aided in data product production (of global maps), science discussions, detailed review, editing
James W. Head: Science discussions, detailed review, editing
Timothy D. Glotch: Science discussion, review, editing
Mackenzie N. White: Copy editing